Azerbaijan Journal of Physics

FİZİKA

3

www.physics.gov.az

E

XXX

2024

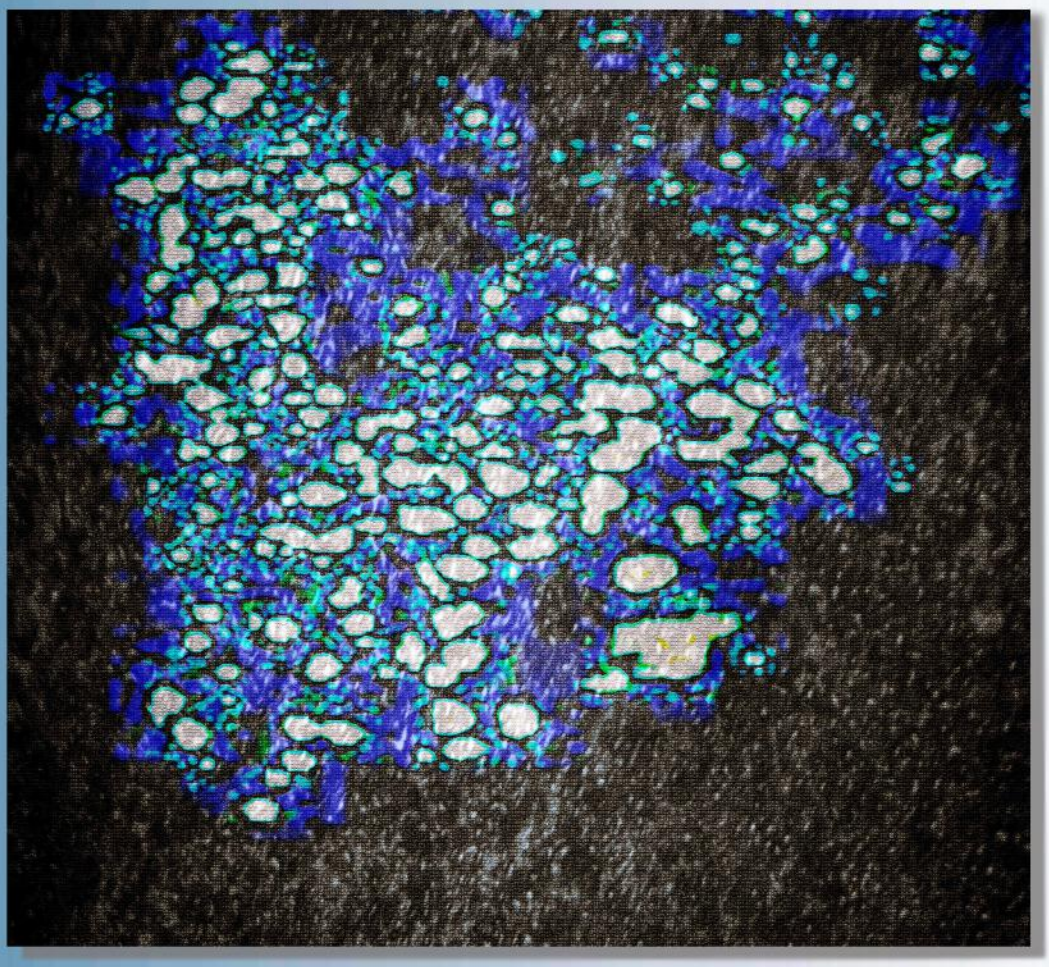

Published from 1995
Ministry of Press and Information
of Azerbaijan Republic,
Registration number 514, 20.02.1995

ISSN 1028-8546
vol. XXX, Number 03, 2024
Section: E

Azerbaijan Journal of Physics

FIZIKA

Ministry of Science and Education Republic of Azerbaijan
Institute of Physics

HONORARY EDITORS

Arif PASHAYEV

EDITORS-IN-CHIEF

Arif HASHIMOV

SENIOR EDITOR

Talat MEHDIYEV

INTERNATIONAL REVIEW BOARD

Arif Hashimov, Azerbaijan
Boris Denker, Russia
Vyacheslav Tuzlukov, Belarus
Gennadii Jablonskii, Belarus
Vladimir Man'ko, Russia
Dieter Hochheimer, USA
Victor L'vov, Israel
Majid Ebrahim-Zadeh, Spain
Natig Atakishiyev, Mexico
Huseyn Ibragimov, Azerbaijan
Nazim Mamedov, Azerbaijan
Anatoly Boreysho, Russia
Mikhail Khalin, Russia
Javad Abdinov, Azerbaijan
Faik Mikailzade, Türkiye
Tayar Djafarov, Azerbaijan
Kerim Allahverdiyev, Azerbaijan
Talat Mehdiyev, Azerbaijan
Zakir Jahangirli, Azerbaijan
Salima Mehdiyeva, Azerbaijan
Nadir Abdullayev, Azerbaijan
Oktay Tagiyev, Azerbaijan
Ayaz Bayramov, Azerbaijan
Tofiq Mammadov, Azerbaijan
Shakir Nagiyev, Azerbaijan
Rauf Guseynov, Azerbaijan

TECHNICAL EDITORIAL BOARD

Senior secretary: Elmira Akhundova; Nazli Huseynova, Elshana Aleskerova, Rena Nayimbayeva, Nigar Aliyeva, Gulnura Jafarova

PUBLISHING OFFICE

131, H. Javid ave., AZ-1143, Baku
Ministry of Science and Education Republic of Azerbaijan
Institute of Physics

Tel.: (99412) 539-51-63, 539-32-23
Fax: (99412) 537-22-92
E-mail: jophphysics@gmail.com
Internet: www.physics.gov.az

It is authorized for printing:

EXACT WAVE FUNCTIONS AND DYNAMICAL SYMMETRY GROUP FOR THE MODIFIED NONRELATIVISTIC RING-SHAPED KRATZER POTENTIAL

SHAKIR M. NAGIYEV, KÖNÜL SH. JAFAROVA, SHOVQIYYA A. AMIROVA, VEFA A. TARVERDIYEVA
Institute of Physics, Ministry of Science and Education,
Javid Ave. 131, AZ 1143, Baku, Azerbaijan
shakir.m.nagiyev@gmail.com, konule2016@gmail.com, shovqiyya@mail.ru, vefa.tarverdiyeva@mail.ru

We propose a new exactly solvable potential which consists of the modified Kratzer potential plus a new ring-shaped potential $(\beta + \gamma\cos\theta + \nu\cos^2\theta)/r^2\sin^2\theta$. The exact solutions of the bound states of the Schrödinger equation for this potential are presented analytically by using the functional method. The wavefunctions of the radial and angular parts are taken on the form of the Laguerre polynomials and the Jacobi polynomials, respectivly. Total energy of the system is different from the modified Kratzer potential because of the contribution of the angular part. We also build a dynamical symmetry group for the radial part of the equation of motion, which allows us to find the energy spectrum purely algebraically.

Keywords: Schrödinger equation; ring-shaped modified Kratzer potential; dynamical symmetry group; Laguerre and Jacobi polynomials.
PACS: 03.65.Ge

1. Introduction

When describing the physical properties of quantum dynamical systems, such as molecules and atoms, atomic nuclei and hadrons, relativistic or non-relativistic potential models play an important role [1-5]. Due to the fact that almost all interactions occurring in nature do not have an obvious type of potential, a model or phenomenological potential is proposed for the study of a quantum system, in which its most essential properties are highlighted and non-existent ones are discarded. Potential models are widely used to study the laws of motion of quantum microparticles in external potential fields (see, for example, [5, 6] and references there)).

The state of a system in quantum mechanics is completely described by the wave function. These states can generally be either bound or scattered states. By solving the corresponding equations of motion (the Schrödinger equation, the Klein-Gordon equation, the Dirac equation or the equation of finite-difference quantum mechanics (see [7] and references there)) within the framework of the potential model, we find an explicit form of the wave function and energy spectrum for these states.

Among quantum mechanical problems, exactly solvable problems occupy a special place. It is well known that the number of potentials allowing an exact solution of relativistic and non-relativistic wave equations is small. These include, for example, Coulomb, harmonic oscillator, Kratzer [4, 8], Hartmann [9], Quesne [10] and Hautot [6] potentials. Some classes of exactly-solvable Klein–Gordon equations are considered in [11].

Note that Hartmann, Quesne and Hautot [6] potentials are non-central potentials. The class of noncentral potentials [6, 7, 9, 10, 12–19] plays a particularly important role in quantum mechanics, nuclear physics, and theoretical chemistry. Non-central or ring-shaped potentials usually consist of two terms

$$V(r,\theta) = V(r) + \frac{f(\theta)}{r^2}, \qquad (1)$$

where is the first term $V(r)$ describes the central field, and the second term $\frac{f(\theta)}{r^2}$ characterizes the ring-shaped potential.

The purpose of this work is to find exact solutions of the Schrödinger equation using functional methods and to construct a dynamic symmetry group for the new ring-shaped modified Kratzer potential of the form

$$V(r,\theta) = D\left(1 - \frac{a}{r}\right)^2 + \frac{\beta+\gamma\cos\theta+\nu\cos^2\theta}{r^2\sin^2\theta}. \qquad (2)$$

Here D is the dissociation energy, a is the equilibrium internuclear separation, and $\beta,\ \gamma,\ \nu$ are the parameters. The first term in (2) involves an attractive Coulomb potential and a repulsive inverse square potential. The second term of (2) describes the annularity of the interaction between the atoms. When $\beta = \gamma = \nu = 0$, the ring-shaped Kratzer potential reduces to a Kratzer potential for which the analytical solutions of the Schrödinger equation are known [4, 12]. The Kratzer potential [4, 12] is widely used in atomic and molecular physics and quantum chemistry. Other varieties of the ring-shaped Kratzer potential were studied in [13, 17].

2. Exact solution of the Schrödinger equation with the ring-shaped modified Kratzer potential

2.1. Separation of variables.

Let us write the Schrödinger equation with potential (2) in a spherical coordinate system

131, H.Javid ave, AZ-1143, Baku
Institute of Physics
E-mail: jophphysics@gmail.com

$$\left\{\frac{1}{r^2}\partial_r(r^2\partial_r)+\frac{\Delta_{\theta,\varphi}}{r^2}+\frac{2m_0}{\hbar^2}\left[E-D\left(1-\frac{a}{r}\right)^2-\frac{f(\theta)}{r^2}\right]\right\}\psi(\mathbf{r})=0, \tag{3}$$

where

$$\Delta_{\theta,\varphi}=\frac{1}{\sin\theta}\partial_\theta(\sin\theta\,\partial_\theta)+\frac{1}{\sin^2\theta}\partial_\varphi^2. \tag{4}$$

equation (3) allows separation of variables. To do this, let's put

$$\psi(\mathbf{r})=R(r)F(\theta,\varphi). \tag{5}$$

After substituting (5) into (3) we obtain two equations:

a) radial Schrödinger equation

$$\frac{d^2R}{dr^2}+\frac{2}{r}\frac{dR}{dr}+\left(\frac{2m_0}{\hbar^2}\left[E-D\left(1-\frac{a}{r}\right)^2\right]-\frac{\Lambda}{r^2}\right)R=0, \tag{6}$$

b) the angular part of the Schrödinger equation

$$\left[\Delta_{\theta,\varphi}-\frac{2m_0}{\hbar^2}f(\theta)+\Lambda\right]F(\theta,\varphi)=0, \tag{7}$$

Here Λ there is a splitting parameter.

2.2. Exact solution of the radial equation.

In equation (6) we move on to the dimensionless variable $\rho=\frac{r}{a}$. In terms ρ equation (6) will take the form

$$R''+\frac{2}{\rho}R'+\left(\frac{2m_0a^2}{\hbar^2}\left[E-D\left(1-\frac{1}{\rho}\right)^2\right]-\frac{\Lambda}{\rho^2}\right)R=0. \tag{8}$$

Here the primes mean differentiation by ρ.

Let us now note that since the limits of potential (2) at $r\to\infty$ and at $r\to 0$ equal

$$\lim_{r\to\infty}V(r,\theta)=V_\infty=D,\qquad \lim_{r\to 0}V(r,\theta)=\infty, \tag{9}$$

then we can say that the energy spectrum at $E<D$ will be discrete, and when $E>D$ will be continuous.

Introducing dimensionless quantities

$$\varepsilon=\frac{2m_0a^2}{\hbar^2}(D-E),\ \ \alpha=\frac{2m_0a^2D}{\hbar^2}, \tag{10}$$

we rewrite equation (8) in the form

$$R''+\frac{2}{\rho}R'+\left(\frac{2\alpha}{\rho}-\frac{\Lambda_1}{\rho^2}-\varepsilon\right)R=0. \tag{11}$$

where $\Lambda_1=\Lambda+\alpha$.

To study equation (11), as usual, we put

$$R(\rho)=\frac{\chi(\rho)}{\rho}. \tag{12}$$

In this case, equation (11) is reduced to the form

$$\chi''+\left(\frac{2\alpha}{\rho}-\frac{\Lambda_1}{\rho^2}-\varepsilon\right)\chi=0. \tag{13}$$

Let us consider separately the cases $\varepsilon>0$ and $\varepsilon<0$.

1) $\varepsilon > 0$ case. Wherein the radial wave function satisfies the boundary conditions

$$\chi(0) = \chi(\infty) = 0. \tag{14}$$

Therefore, at small ρ the solution is proportional ρ^s. At large ρ we get the equation

$$\chi'' - \varepsilon\chi = 0, \tag{15}$$

whence, taking into account (14), we have $\chi = e^{-\sqrt{\varepsilon}\rho}$.

Therefore, in (13) it is natural to make the substitution

$$\chi = \rho^s e^{-\sqrt{\varepsilon}\rho}\Omega(\rho) \equiv g(\rho)\Omega(\rho), \tag{16}$$

where $s = \frac{1}{2} + \sqrt{\frac{1}{4} + \Lambda_1}$. If the coefficients of equation (13) are denoted by $a_2 = 1,\ a_1 = 0,\ a_0 = \frac{2\alpha}{\rho} - \frac{\Lambda_1}{\rho^2} - \varepsilon$, then the function Ω will satisfy the equation

$$b_2\Omega'' + b_1\Omega' + b_0\Omega = 0, \tag{17}$$

where

$$b_2 = a_2, b_1 = a_1 + 2a_2\frac{g'}{g}, b_0 = a_0 + a_1\frac{g'}{g} + a_2\frac{g''}{g}. \tag{18}$$

Now equation (17) takes the form

$$\rho\Omega'' + \left(2s - 2\sqrt{\varepsilon}\rho\right)\Omega' + \left(2\alpha - 2s\sqrt{\varepsilon}\right)\Omega = 0 \tag{19}$$

After changing the variable $\rho = t/2\sqrt{\varepsilon}$ we get

$$t\Omega''(\mathrm{t}) + (2\mathrm{s} - \mathrm{t})\Omega'(\mathrm{t}) + \left(\frac{\alpha}{\sqrt{\varepsilon}} - \mathrm{s}\right)\Omega(\mathrm{t}) = 0 \tag{20}$$

Comparing this equation with the equation for Laguerre polynomials [20] $y = L_n^{\lambda}(x)$:

$$xy'' + (\lambda + 1 - x)y' + ny = 0, \tag{21}$$

we find that

$$\lambda = 2s - 1,\ n = \frac{\alpha}{\sqrt{\varepsilon}} - s,\ n = 0,1,2, \ldots$$

The last condition leads to energy quantization equation

$$E_n = D - \frac{2m_0a^2D^2}{\hbar^2}\left[n + \frac{1}{2} + \sqrt{\frac{1}{4} + \frac{2m_0a^2D}{\hbar^2} + \Lambda}\right]^{-2}, \tag{22}$$

and the function $\Omega(\mathrm{t})$ coincides with the Laguerre polynomial

$$\Omega(\mathrm{t}) = L_n^{2\mathrm{s}-1}(t) = L_n^{2\mathrm{s}-1}\left(\frac{2\alpha\rho}{n+s}\right). \tag{23}$$

Therefore the radial wave function

$$R_{n\Lambda}(r) = C_{n\Lambda}\rho^{s-1}e^{-\sqrt{\varepsilon_n}\rho}L_n^{2\mathrm{s}-1}\left(\frac{2\alpha\rho}{n+s}\right). \tag{24}$$

Note that the parameter Λ we find from the solution of the angular part of the Schrödinger equation (7).

2.3. Dynamical symmetry group $\mathbf{SU(1,1)}$

Let us now consider the radial equation (11) by the help of $\mathrm{SU}(1,1)$ Lie algebra. The generators of $\mathrm{SU}(1,1)$ algebra may be realized as [21]

$$K_0 \equiv \Gamma_0 = \frac{1}{2}\left(-\rho\partial_\rho^2 - 2\partial_\rho + \frac{\Lambda_1}{\rho} + \rho\right),$$
$$K_1 \equiv \Gamma_4 = \frac{1}{2}\left(-\rho\partial_\rho^2 - 2\partial_\rho + \frac{\Lambda_1}{\rho} - \rho\right), \tag{25}$$
$$K_2 \equiv T = -i\left(\rho\partial_\rho + 1\right),$$

By a direct check, one can verify that these operators satisfy the commutation relations

$$[\Gamma_0, \Gamma_4] = iT, [T, \Gamma_0,] = i\Gamma_4, [\Gamma_4, T] = -i\Gamma_0. \tag{26}$$

The casimir operator is $C_2 = \Gamma_0^2 - \Gamma_4^2 - T^2 = \mu(\mu - 1)$, where $\mu > 0$ is an eigenvalue of the operator C_2.

We denote that states of a positive discrete series as $|n,\mu >$, $n = 0,1,2, \dots$, such that

$$\Gamma_0|n,\mu > = (n + \mu)|n,\mu >,$$
$$C_2|n,\mu > = \mu(\mu - 1)|n,\mu >. \tag{27}$$

It should be noted that in our case from equation (25), we obtain $C_2 = \Lambda_1 = \mathrm{s}(\mathrm{s} - 1)$, so $\mu = s$. Equation (11) can be written with the help of generators (25) as

$$[(1 + \varepsilon)\Gamma_0 + (1 - \varepsilon)\Gamma_4 - 2\alpha]R = 0. \tag{28}$$

Let us introduce a new parameter λ and perform a tilting transformation

$$\tilde{R} = e^{-i\lambda T}R. \tag{29}$$

To solve this equation algebraically, we use the formulas

$$e^{-i\lambda T}\Gamma_0 e^{i\lambda T} = \Gamma_0 \mathrm{ch}\lambda + \Gamma_4 \mathrm{sh}\lambda,$$
$$e^{-i\lambda T}\Gamma_4 e^{i\lambda T} = \Gamma_4 \mathrm{ch}\lambda + \Gamma_0 \mathrm{sh}\lambda. \tag{30}$$

As a result, for the function $\tilde{R}$ (29) we get the equation

$$(b\Gamma_0 + c\Gamma_4 - 2\alpha)\tilde{R} = 0, \tag{31}$$

where

$$b = (1 + \varepsilon)\mathrm{ch}\lambda + (1 - \varepsilon)\mathrm{sh}\lambda,$$
$$c = (1 + \varepsilon)\mathrm{sh}\lambda + (1 - \varepsilon)\mathrm{ch}\lambda.$$

We consider separately the cases when $E < D$ and $E > D$.

1) When $E < D$(discrete spectrum) in (31), a compact generator Γ_0 can be diagonalized [20]. Setting $c = 0$, we obtain $\mathrm{th}\lambda = (1 + \varepsilon)(1 - \varepsilon)$. As a result, we have $b = 2\sqrt{\varepsilon}$ and

$$\left(2\sqrt{\varepsilon}\Gamma_0 - 2\alpha\right)\tilde{R} = 0. \tag{32}$$

It follows from (32) the energy equation (22).

2) When $E > D$, noncompact generator Γ_4 is diagonalized, having a continuous real spectrum $\delta \in R$. In this case $b = 0$ and we have $\mathrm{th}\lambda = -(1 + \varepsilon)/(1 - \varepsilon)$. As a result we have $c = 2\sqrt{\varepsilon}$ and

$$\left(2\sqrt{-\varepsilon}\Gamma_4 - 2\alpha\right)\tilde{R}_1 = 0. \tag{33}$$

Consequently, $\frac{\alpha}{\sqrt{-\varepsilon}} = \delta$ or

$$E_\delta = D + \frac{2m_0 a^2 D^2}{\hbar^2\delta^2}. \tag{34}$$

3. The solutions of the angular equation

We now find the solutions the angle-dependent equation (7). The variables in (7) can be separated in the usual way

$$F(\theta, \varphi) = \Theta(\theta)\frac{e^{im\varphi}}{\sqrt{2\pi}}. \tag{35}$$

Here, m is the usual magnetic quantum number and is integer. Equation for $\Theta(\theta)$ now looks like

$$\left(\partial_\theta^2 + \mathrm{ctg}\theta\partial_\theta - \frac{m'^2+\gamma_0\cos\theta+\nu_0\cos^2\theta}{\sin^2\theta} + \Lambda\right)\Theta(\theta) = 0. \tag{36}$$

The orthonormalized solutions of this equation were found in [7]. We give here their explicit form

$$\Theta_{km}(\theta) = \mathrm{c}_{km}\left(\sin^2\frac{\theta}{2}\right)^{A_1}\left(\cos^2\frac{\theta}{2}\right)^{A_2} P_k^{(2A_1,2A_2)}(\cos\theta), \tag{37}$$

where $k = 0,1,2,\ldots$, the functions $P_k^{(\alpha,\beta)}(x)$ are the Jacobi polynomials [21] and the positive parameters $A_{1,2}$ are

$$A_{1,2} = \frac{1}{2}\sqrt{m^2+\nu_0+\beta_0 \pm \gamma_0}. \tag{38}$$

Normalization coefficients

$$c_{km} = \sqrt{\frac{(k+A_1+A_2+1/2)k!\Gamma(k+2A_1+2A_2+1)}{\Gamma(k-2A_1+1)\Gamma(k-2A_2+1)}} \tag{39}$$

are determined from the normalizing condition for the angular wave functions (37)

$$\int_0^\pi \Theta_{km}(\theta)\,\Theta_{k'm}(\theta)\sin\theta d\theta = \delta_{kk'}\ . \tag{40}$$

As shown in [7], the separation constant Λ depends on k and m

$$\Lambda \equiv \Lambda_{\mathrm{km}} = \mathrm{k}\left[\mathrm{k}+1+\sqrt{\mathrm{m}^2+\nu_0+\beta_0+\gamma_0}+\sqrt{\mathrm{m}^2+\nu_0+\beta_0-\gamma_0}\right]+$$
$$+\frac{1}{2}\left[\sqrt{\mathrm{m}^2+\nu_0+\beta_0+\gamma_0}+\sqrt{\mathrm{m}^2+\nu_0+\beta_0-\gamma_0}\right]+$$
$$+\ \frac{1}{2}\sqrt{(\mathrm{m}^2+\nu_0+\beta_0+\gamma_0)(\mathrm{m}^2+\nu_0+\beta_0-\gamma_0)}+\frac{1}{2}(\mathrm{m}^2+\beta_0-\nu_0) \tag{41}$$

Thus, the exact discrete energy eigenvalues of the Schrödinger equation for our quantum system are (see, (22) and (41))

$$E_{nkm} = D - \frac{2m_0a^2D^2}{\hbar^2}\left[n+\frac{1}{2}+\sqrt{\frac{1}{4}+\Lambda_{\mathrm{km}}+\frac{2m_0a^2D}{\hbar^2}}\right]^{-2}, \tag{42}$$

where $n = 0,1,2,\ldots$, $k = 0,1,2,\ldots$, $m = 0,\pm1,\pm2,\ldots$

We consider a special case of the formula (42). For $f(\theta) = 0$ will have a results of the paper [12].

4. Conclusion

In this paper, we considered an exactly solvable model, namely a non-relativistic ring-shaped modified Kratzer potential model.

The main results of this paper are the explicit and exact expressions for the energy spectrum and corresponding wave functions. We have also find the dynamical symmetry group $SU(1,1)$.

[1] *L.D. Landau, E.M. Lifshitz.* Quantum Mechanics 3rd edn. (Pergamon Press, 1979).

[2] *A.S. Davydov.* Quantum Mechanics (Pergamon Press, 1965).

[3] *W. Greiner.* Relativistic Quantum Mechanics 3rd edn. (Springer, 2000).

[4] *S. Flügge.* Practical Quantum Mechanics Vol. 1 (Springer, 1994).

[5] *V.G. Bagrov, D.M. Gitman.* Exact Solutions of Relativistic Wave Equations (Kluwer Academic Publishers, 1990).

[6] *A. Hautot.* Exact motion in noncentral electric felds. J. Math. Phys. 14(10), 1320–1327 (1973).

[7] *Sh.M. Nagiyev, A.I. Ahmadov*. Exact solution of the relativistic fnite diference equation for the Coulomb plus Ring-Shaped potential. Int. J. Mod. Phys. A 34(17), 1950089 (2019).

[8] *A. Kratzer*. Die ultraroten Rotationsspektren der Halogenwasserstofe. Z. Phys. 3(5), 289–307 (1920).

[9] *H. Hartmann.* Die Bewegung eines Körpers in einem ringförmigen Potentialfeld. Teor. Chim. Acta 24(2–3), 201–206 (1972).

[10] *C.J. Quesne*. A new ring-shaped potential and its dynamical invariance algebra. Phys. A: Math. Gen. 21, 3093–3103 (1988).

[11] *De Souza Dutra, G. Chen*. On some classes of exactly-solvable Klein–Gordon equations, Phys. Lett. A 349 (2006) 297 – 301.

[12] *C. Berkdemir, A. Berkdemir and J.G. Han.* Bound state solutions of the Schrödinger equation for modified Kratzer molecular potential, Chem. Phys. Lett. 417, 2006, 326.

[13] *Y.F. Cheng, T.Q. Dai.* Exact solution of the Schrödinger equation for modified Kratzer potential plus a ring-shaped potential by the Nikiforov – Uvarov methad, Phys. Scr. 75 (2007) 274 – 277.

[14] *C.Y. Chen, S.H. Dong*. Exactly complete solutions of the Couloumb potential plus a new ring-shaped potential, Phys. Lett. A 335 (2005) 374-382.

[15] *C.Y. Fu, D.T. Qing.* Exact solutions of the Schrödinger equation for a new ring-shaped nonharmonic oscillator potential. Int. J. Mod. Phys. A 23 (2008) 1919-1927.

[16] *K.J. Oyewumi*. Analytical solutions of the Kratzer-Fues potential in an arbitrary number of dimensions, Found. Phys. Lett. 18 (2005) 75 – 84.

[17] *A. Durmus, F. Yasuk.* Relativistic and nonrelativistic solutions for diatomic molecules in the ppresence of double ring-shaped Kratzer potential, J. Chem. Phys. 126, 074108 (2007).

[18] *Sh.M. Nagiyev, A.I. Ahmadov, A.N. Ikot, V.A.Tarverdiyeva.* Analytic solutions for the Klein-Gordon equation with combined exponential type and ring-shaped potentials, Scientific Rep., (2024) 145527.

[19] *S.M.Nagiyev,A.I.Ahmadov, V.A.Tarverdiyeva*. Approximate solutions to the Klein–Fock–Gordon equation for the sum of coulomb and ring-shaped-like potentials. Adv. High Energy Phys. 2020, 1356384 (2020).

[20] *R. Koekoek, P. A. Lesky and R. F. Swarttow*. Hypergeometric Orthogonal Polynomials and their q-Analogues (Springer-Verlag, Berlin, 2010).

[21] *A.O. Barut and R. Raczka.* Theory of Group Representations and Applications (Polish Scientific Publishers, Warszawa, 1977).

Received: 08.07.2024

OPTICAL PROPERTIES OF SEMICONDUCTOR SUPERLATTICES (REVIEW)

S.A. ZALOVA
Ministry of Science and Education, Institute of Physics
AZ 1143, Azerbaijan, Baku, H.Javid ave.,131
zalova0300@gmail.com

The optical properties of semiconductor superlattices are considered - solid-state structures in which, in addition to the periodic potential of the crystal lattice, there is an additional one-dimensional potential, the period of which significantly exceeds the lattice constant.

Keywords: semiconductor superlattice, absorption coefficient, Wannier-Stark energy level, magnetophonon resonance.
PACS: 78.55;73,22.CD,7322.

The progress of solid-state electronics is driven by research in the field of creating materials with new, sometimes unusual, properties. One such material is a superlattice (SL). Semiconductor superlattices are nanostructures consisting of alternating layers of two distinct semiconductor materials, such as GaAs and (AlGa)As, which often have extremely comparable lattice constants [1]. Interest in SL is primarily due to the fact that electronic energy. The spectrum of SL can be controlled to a certain extent at the stage of its creation. Presence of superlattice potential significantly changes the energy spectrum, due to which superlattices have a number of interesting properties that are absent in conventional semiconductors. The parameters of the superlattice potential can be easily changed over a wide range, which in turn leads to significant changes in the energy spectrum. Thus, it is easy to change the band structure of semiconductor superlattices. The parameters of the superlattice potential can be easily changed over a wide range, which in turn leads to significant changes in the energy spectrum. Thus, it is easy to change the band structure of semiconductor superlattices.

Explosive growth of both theoretical and experimental interest to superlattices is associated with the latest advances in technology based on molecular beam epitaxy in ultra-high vacuum, also reviews as well as metal-organic epitaxy from the gas phase and other methods.

Due to a number of quantum mechanical phenomena, such as resonant tunneling, the development of Wannier-Stark energy level ladders, and the occurrence of Bloch oscillations [1, 2], whose frequency is proportional to the spatial period, d, of the SL as well as to F, the current-voltage characteristics of semiconductor superlattices are typically highly nonlinear. Bloch oscillations do not occur in natural crystals because *d* is so small (~ 0.3 nm), meaning that the Bloch frequency is substantially smaller than the electron scattering rate. However, in semiconductor superlattices, *d* and the associated Bloch frequency can be large enough for the electrons to oscillate in a Bloch fashion, which is then important for the high-frequency charge transport process as well as the dc one. As the electric field increases, the drift (average) velocity of the electrons decreases due to the localization caused by the commencement of Bloch oscillations.

However, difficulties in experimental obtaining high-quality SL samples led to the fact that the theoretical study of SL [3] began long ago before the appearance of the first experimental samples of satisfactory quality, obtained on the basis of $GaAs/Al_xGa_{1-x}As$ by epitaxy from molecular bunches. In particular, in [3,4] it was proposed SL energy spectrum in the one-miniband approximation

$$\varepsilon(\vec{p}) = \frac{p_y^2+p_z^2}{2m} + \Delta\{1-\cos(\mathrm{p_x d}/\hbar)\} \quad (1)$$

where m is the effective mass of the electron in the ZOY plane, A is the half-width of the conduction miniband, *d* - period SR. In this case, it is assumed that CP is periodic along the OX axis, P_x, P_y, P_z are the components of the quasi-momentum electron on the coordinate axis.

Figure 1 shows the superlattice structure and band structure. We can see that GaAs and AlAs will form a potential well, as shown in figure 1(b), this is because of the different band gap in these two materials. Furthermore, the motion of the charged carrier in superlattice quantum wells will be effected by potential barriers on both side of the potential well, so that it will be hindered We consider the transport of an electron gas in a semiconductor superlattice with a periodical potential well *U(z)* along the *z* direction under the influence of a constant magnetic field *B=B//z*. The one-particle Hamiltonian describing an electron in a semiconductor superlattice is then given by

$$\mathrm{H} = \frac{1}{2\mathrm{m}^*}(\mathrm{p}+\mathrm{eA})^2 + \mathrm{U(z)} + \mathrm{g}^*\mu_\mathrm{B}\sigma\cdot\mathrm{B} \quad (2)$$

The electron wave function and the eigenvalues, *E*, of Eqs. (3), (4) and (5) in the conduction band are expressed as

$$\langle x,y.z|\lambda\rangle = \psi_{n,}k_{x,}k_{z,\sigma}(x,y,z) = \frac{1}{\sqrt{L_x}}exp[ik_x x]u_{n,k_x}(y)\xi_z\,(z)\chi_\sigma \quad (3)$$

with

131, H.Javid ave, AZ-1143, Baku
Institute of Physics
E-mail: jophphysics@gmail.com

$$u_{n,k_x}(y) = \left(\frac{1}{2^n n!\,\sqrt{\pi} l_B}\right)^{1/2} \times exp\left[-\frac{(y-y_0)^2}{2l_B^2}\right] H_n\left(\frac{y-y_0}{l_B}\right) \quad (4)$$

$$E_\lambda = E_{n,\sigma}(k_x, k_y) = \left(n + \frac{1}{2}\right)\hbar\omega_c + \varepsilon_{SL}(k_z) + \sigma g^* \mu_B B \quad (5)$$

The conduction electrons within the semiconductor superlattices layers may experience high-frequency collective oscillations due to this negative differential velocity [3], which makes semiconductor superlattices appealing for the production and detection of electromagnetic radiation in the GHz to THz frequency range [5, 6, 7]. Negative differential velocity for electrons in superluminate have also given rise to essentially new charge transport regimes including deterministic chaos, which are typified by intricately erratic electron dynamics. [1, 8, 9]. It offers a sensitive new method of regulating electron transport and defies the Kolmogorov-Arnold-Moser (KAM) theorem. Surprisingly, the effective classical Hamiltonian for the electron motion in a semiconductor superlattice depends explicitly on the miniband's energy versus wavevector dispersion relation, indicating that it has an underlying quantum-mechanical foundation [13,14].

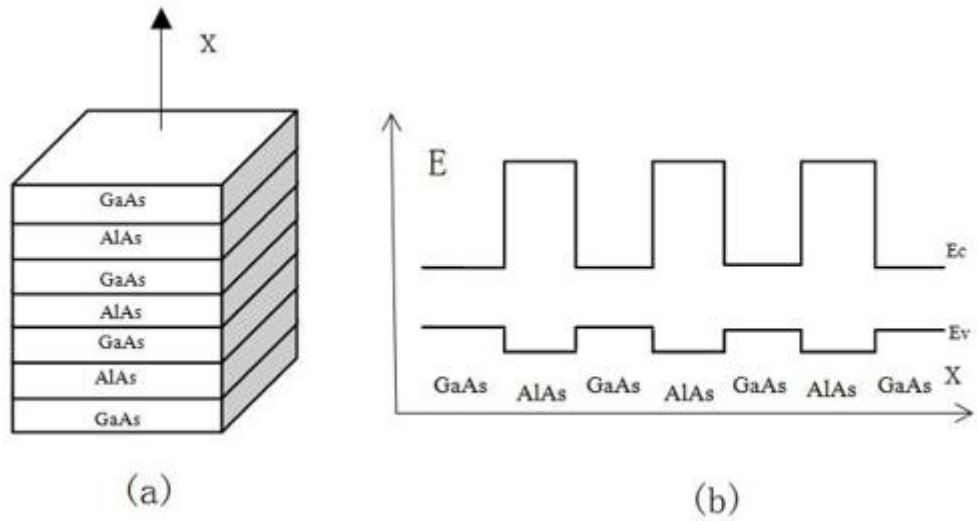

Fig. 1. (a) Schematic of the superlattice structure. (b) Schematic of the band structure of the conduction band the valence band.

The stochastic electron motion turns on abruptly when the field parameters meet specific resonance criteria, which are explained in more detail below, according to an analysis of Hamilton's equations. By leaving an intricate web of conduction channels in phase space—also referred to as a "stochastic web"—the beginning of chaos delocalizes the electrons and results in a significant resonant amplification of the electron velocity and current flow as observed in experiment [14]. This phase-space patterning works even at room temperature [14], and it offers a radically novel idea for regulating electrical conductance [20]. The resonant delocalization of the conduction electrons would result in a sequence of delta-function peaks in the I(V) curves in the absence of dissipation. However, in actual semiconductor superlattices, the resonances are widened because the electrons scatter inelastically via the tunnel walls and quantum well interface roughness as well as elastically [1], primarily because of ionized donor atoms. To get I(V) curves that correspond with experiment, the influence of scattering on the electron dynamics must be considered while computing the transport characteristics of the semiconductor superlattices.

In work [21] investigated how dissipation affects electron transport in a semiconductor superlattice under the influence of a magnetic field that is oriented perpendicular to the superlattice axis and an applied bias voltage. In this work demonstrated that the applied fields, despite being stationary, behave as a THz plane wave, closely coupling electron Bloch and cyclotron motion inside the lowest miniband. This leads to a special kind of Hamiltonian chaos in the electrons, which in turn forms a complex network of conduction channels (a stochastic web) in phase space. At critical values of the applied voltage, this produces a significant resonant increase in the current flow. This patterning in phase-space offers a delicate way to regulate electrical resistance. In this work, introduced a linear damping term into the semiclassical equations of motion to examine the impact of dissipation on the electron dynamics. It is shown that deterministic chaos contributes significantly to the electron transport process even when dissipation is present. Complex multistability phenomena arises in the system when the cyclotron and Bloch frequencies are comparable. Specifically, multiple separate stable regimes can coexist for fixed values of the control parameters, each

of which corresponds to a different initial condition. In this work is demonstrated that the electron transport properties clearly exhibit the fingerprints of this multistability, as observed experimentally.

Semiconductor materials have been widely used in electronics in recent years. The phenomena of contact p-n and the doped capacity to change the physical characteristics of crystals are the fundamental driving forces behind the development of semiconductor electronics. As a result, many scientists are now interested in the magneto-thermoelectric effects in low-dimensional systems. In [22] investigates the impact of Ettingshausen in semiconductors when laser radiation is present. The findings demonstrate that the degree of these "photostimulated" effects can be greater than the similar effects when radiation is not present. The EC in bulk semiconductors is expressed analytically in [22], which also demonstrates how the Ettingshausen coefficient depends on lattice heat conductivity, radiation frequency, and the amplitude of the laser radiation field conductivity.

In [23], the Boltzmann kinetic equation was utilized to investigate the Ettingshausen effect in compositional semiconductor superlattices caused by an electric field. The outcome demonstrates how the Ettingshausen effect is affected by magnetic and electric fields, as well as how it may be possible to increase (transverse) thermoelectric effectivity at the expense of electric fields.

In work [24] is investigated magneto-thermoelectric effects in the doped semiconductor superlattice under the impact of electromagnetic waves using a quantum kinetic equation for electrons. We have also determined analytical expressions of the Ettingshausen coefficient in doped semiconductor superlattice for the electron-acoustic phonon interaction. Compared to the expressions found in the case of bulk semiconductors, these expressions are significantly different. They observed that the Ettingshausen coefficient relies on the temperature, the characteristic parameters of doped semiconductor superlattice, and the characteristic parameters of electromagnetic waves. The results are computed numerically for the GaAs:Be/GaAs:Si doped semiconductor superlattice. The findings align with recent experimental findings; nonetheless, the Ettingshausen coefficient differs from that of bulk semiconductors or bismuth.

Using canonical ensemble statistics for under a tilted magnetic field, investigated the orbital magnetization and heat capacity of an electron system analytically and quantitatively [25]. For a bulk semiconductor superlattice, the orbital magnetization and heat capacity are obtained as functions of the magnetic field intensity at finite temperature. In addition, the calculations are made for the orbital magnetization, heat capacity, temperature, and tilt angle of the slanted magnetic field.

The Hall effect in doped semiconductor superlattices (DSSL) under the impact of restricted LO-phonons and laser radiation has been theoretically investigated based on the quantum kinetic equation technique [26]. The Hall coefficient, magnetoresistance, and Hall conductivity tensor of a GaAs:Si/GaAs are expressed analytically as follows: In terms of the doping concentration, lattice period and external fields, DSSL is achieved. The effect of electron and LO-phonon confinement was characterized by varying the quantum numbers N, n, and m. When compared to the case of bulk phonons, numerical evaluations demonstrated that LO-phonon confinement increased the probability of electron scattering, increasing the number of resonance peaks in the Hall conductivity tensor and decreasing the magnitude of both the magnetoresistance and the Hall coefficient, in contrast to the situation of bulk phonons. It was discovered that the magnetoresistance's nearly linear temperature increase matched the experiment fairly well. Figure 2 shows the dependence of the conductivity tensor s_{xx} on the cyclotron energy for confined phonon and bulk phonon.

It is commonly recognized that, in low-dimensional semiconductor systems, the effect of phonon confinement alters the probability of carrier scattering, resulting in unique material behaviors relative to the case of unconfined phonons [27, 28]. As a result, numerous published works have explored the impact of confined phonons on the optical, electrical, and magnetic characteristics of low-dimensional semiconductor systems. These include the impact of confined phonons on carrier capture processes [30], the absorption coefficient of strong electromagnetic waves [29], and the resonant quasi-confined optical phonons in semiconductor superlattices [31]. The branches of optical phonons in semiconductor systems are limited when they do not overlap; the confined optical phonon's wave vector contains both the quantized and in-plane components [27, 32]. The guided mode model, the slab mode model, and the Huang-Zhu model are examples of diverse confined phonon models that result from the various boundary conditions applied to the electrostatic potential or vibrational amplitude of the phonons [33]. We have examined the Hall effect in doped semiconductor superlattices (DSSL) with bulk phonons in the earlier study [8]. It has been demonstrated via the studies of [28, 29,32] that phonon confinement plays a significant role in the characteristics of low-dimensional semiconductor systems and shouldn't be disregarded. Using the quantum kinetic equation technique, the analytical formulations of the Hall conductivity tensor, the magnetoresistance, and the Hall coefficient in DSSLs under the effect of confined LO-phonons are found [29, 34].

For nonpolar optical phonons, in [35] derived the longitudinal magnetoconductivity of superlattices. The plateau condition that appears in superlattices is obtained analytically from the relaxation rates which are intimately associated with the magnetophonon resonance. The temperature and miniband width are taken into consideration while examining the qualitative aspects of the magnetophonon resonance, magnetophonon resonance effects. Specifically, the magnetophonon resonance line form behaviors are explored in detail, including the emergence of the

plateau between nearby magnetophonon resonance peaks, the removal of magnetophonon resonance peaks, and variations in the magnetophonon resonance amplitude. Their findings align well with current experimental and theoretical findings.

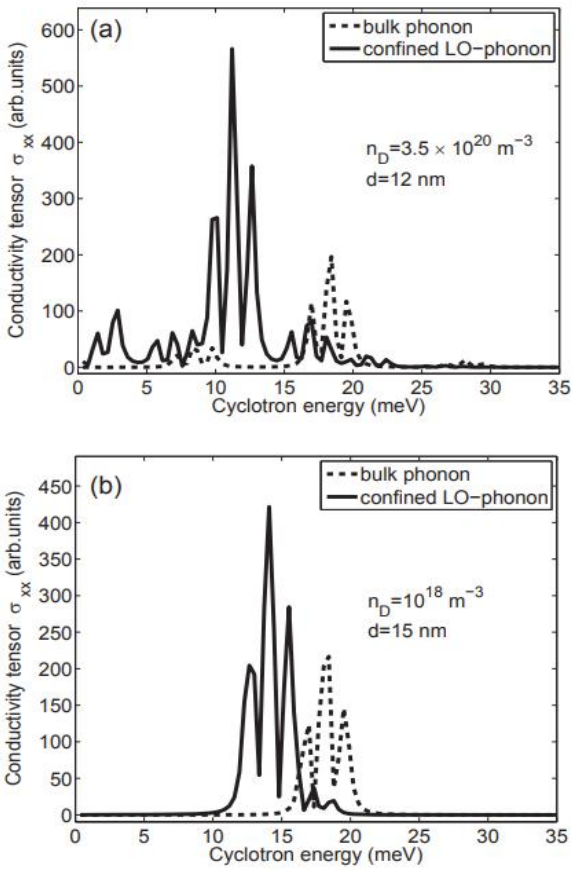

Fig. 2. The dependence of the conductivity tensor s_{xx} on the cyclotron energy for confined phonon (solid curve) and bulk phonon (dashed curve), here *d* =12 nm (fig. 1a) and *d* =15 nm (fig. 1b) [26].

There have been numerous reports of magnetophonon resonance effects investigations in these kinds of systems [36,37.38-41]. Noguchi et al. [39] regarding the magnetophonon resonance in short-period semiconductor superlattices. Their findings for the longitudinal magnetoresistance in GaAs/Al_xGa_{1-x} As superlattices under strong magnetic fields parallel to the electronic fields and normal to the interfaces were reported. Their findings showed that in short-period superlattices, unusual behaviors of the magnetophonon resonance line shape were observed, including the emergence of a plateau between neighboring magnetophonon resonance peaks and the removal of magnetophonon resonance peaks. The energy dispersion relation and the plateau condition derived from the density of states provided an explanation for them. A thorough theoretical analysis of the miniband transport of electrons in a GaAs-based superlattice under the effect of a quantizing magnetic field normal to the layer plane was recently reported by Shu and Lei [40]. More recently, Gassot et al. [41] reported the temperature, pressure, miniband, and electric field dependences of magnetophonon resonance in superlattices and observed strong oscillations of magnetophonon resonance in the background of the longitudinal magnetoconductance in short-period GaAs/AlAs superlattices resulting from electron interactions with both GaAs and AlAs longitudinal optical (LO) phonons. The goal of this work is to derive the plateau for the nonlinear dc conductivity using the linear response limit of a generic equation previously developed, to present a systematic theoretical analysis of miniband electron transport in such a system, to obtain analytically the plateau condition for a GaAs-based superlattice under the influence of a quantizing magnetic field normal to the layer plane and to compare with the theoretical and experimental results reported by some authors [39–41].

In bulk semiconductors, the magnetophonon resonance (MPR) phenomenon has drawn a lot of interest from both practical and theoretical perspectives since it was first predicted by Gurevich and Firsov [42]. There have been numerous reports of MPR impact research in such low-dimensional electronic devices [43–51]. On the other hand, short-period superlattices have received less attention. Noguchi et al. [52] carried out research on MPR in semiconductor superlattices in 1992. Their findings of longitudinal magnetoresistance in GaAs/Al_xGa_{1-x} As superlattices under strong magnetic fields parallel to the electric fields and normal to the interfaces have been presented. Shu and Lei [53] recently provided a systematic theoretical analysis of miniband transport of electrons in a GaAs-based superlattice under the influence of a quantized magnetic field normal to the layer plane. They also observed strong oscillations of MPR on the background of the longitudinal magnetoconductance in short-period GaAs/AlAs superlattices, which are caused by electron interactions with both GaAs and AlAs LO phonons. In work [50], find that as the applied magnetic fields' tilt angle increases, the MPR peak positions of the GaAs and AlAs LO phonon modes shift to regions of higher magnetic strength, while the second derivative of the magnetoconductivities—which includes a miniband width and a potential periodicity—declines and disappears under the same experimental conditions [41]. We contrast our findings with the theoretical and experimental findings reported by a few writers [52-54]. Since its initial prediction by Gurevich and Firsov [42], the magnetophonon resonance (MPR) phenomena in bulk semiconductors has attracted considerable attention from both theoretical and practical standpoints.

The angular dependence of magnetophonon resonance (MPR) peaks for longitudinal optical (LO) phonons in a tilted magnetic field applied to the superlattice axis is obtained from the longitudinal magnetoconductivities of GaAs/AlAs semiconductor superlattices. Using the second derivative of the magnetoconductivities, which includes a miniband width and a potential periodicity, the MPR peaks of the LO phonon modes in both GaAs and AlAs are displayed. The MPR peak placements shift to regions of higher magnetic strength as the tilt angle of the

applied magnetic fields increases, but the peak amplitudes decrease and eventually vanish under the same conditions in the tests. Our findings qualitatively match the experimental findings quite well. As a function of the tilt angles, we also obtain the resonance fields for the MPR peak numbers of the GaAs and AlAs LO phonon modes. In order to explain the emergence of a plateau zone between adjacent peak amplitudes, we also derive the dispersion relations and the density of states (DOS), which include a miniband width, a periodicity of the potential, and tilt angles of the slanted magnetic fields. The plateau area can be elucidated by phenomena like the second derivative of the magnetoconductivity of GaAs/AlAs semiconductor superlattices for tilt angles of the applied magnetic fields and the shifts, decreases, and disappearances of the peak amplitudes of the magnetoconductivities [55]. Fig. 3 and fig.4 shows angular dependence of the frequency-dependent magnetoconductivity $\bar{\sigma}_{zz}(\omega)$ for LO phonon scattering of a Ge-based semiconductor superlattice.

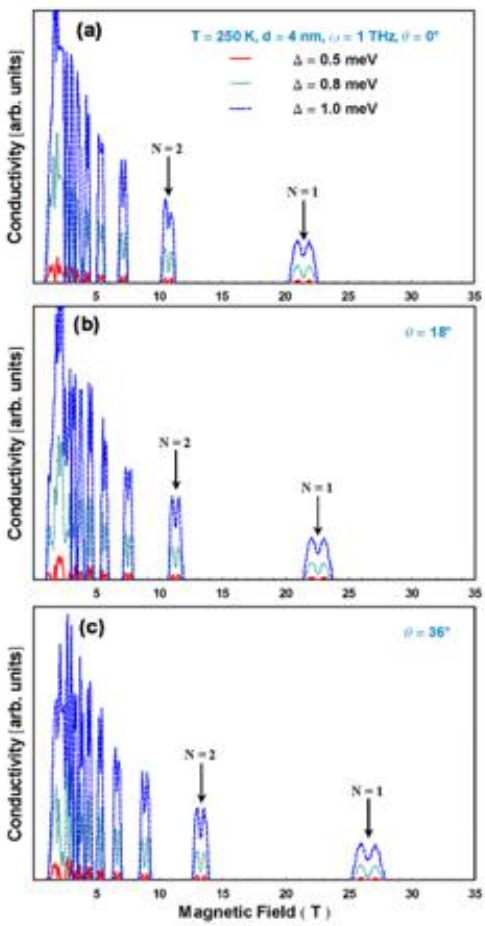

Fig. 3. Angular dependence of the frequency-dependent magnetoconductivity $\sigma_{zz}(\omega)$ for LO phonon scattering of a Ge-based semiconductor superlattice with a photon frequency of ω = 1 THz as a function of the magnetic field strength at T = 250 K. The solid, dotted, and dashed lines are for Δ = 0.5 meV, 0.8 meV, and 1.0 meV, respectively [55].

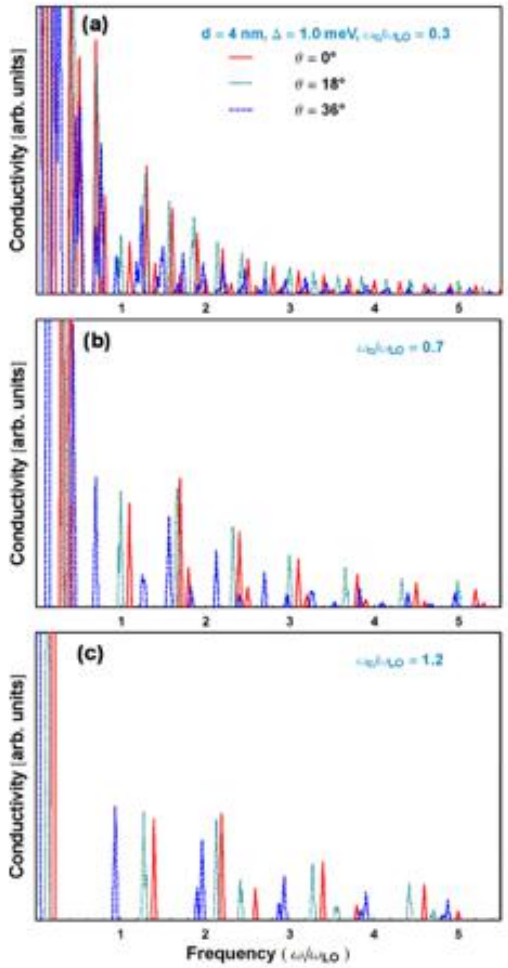

Fig. 4. Angular dependence of the frequency-dependent magnetoconductivity $h\sigma_{zz}(\omega)$ for LO phonon scattering of a Ge-based semiconductor superlattice with a miniband width Δ=1.0 meV at T = 250 K. The solid, dotted, and dashed lines are for θ = 0°, 18°, and 36°, respectively [55].

Based on both Wannier-Stark quantum transport theory and the Landau levels obtained when using magnetic and steady strong electric fields parallel to the axis of the semiconductor superlattice (see fig.5), respectively, we were able to derive the conditions for the Wannier-Stark magnetophonon resonance from the electric conductivity and a relaxation function, which are functions of the temperature, the period of the superlattice, the miniband width, the electron density, and the magnetic and electric fields. Numerical research was done on the behaviors of the line shapes derived from the Wannier-Stark magnetophonon resonance of the relaxation function and the electric conductivity as functions of the phonon energy, electric field, and magnetic field. With increasing electron transitions between the Wannier-Stark and Landau levels, the number of resonance peaks was reduced [56]. Fig. 6 shows electric conductivity σ_{zz} as a function of the electric field for various periods and miniband widths in semiconductor superlattices

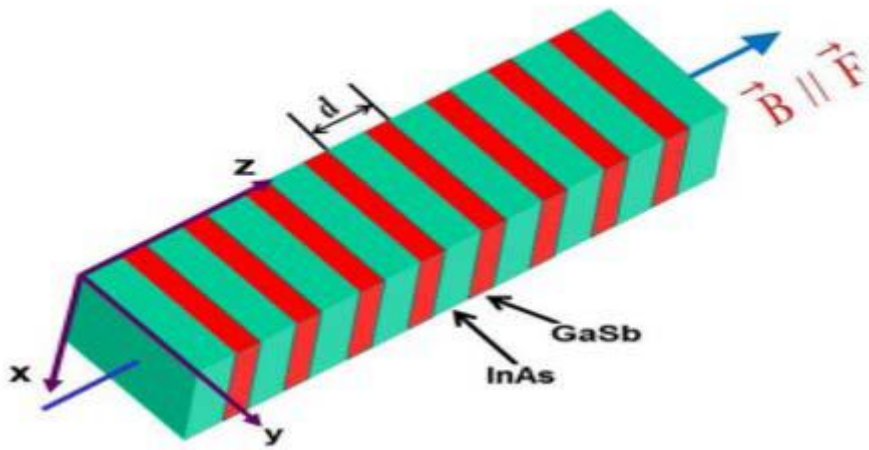

Fig. 5. Schematic illustration of an InAs/GaSb semiconductor superlattice [56].

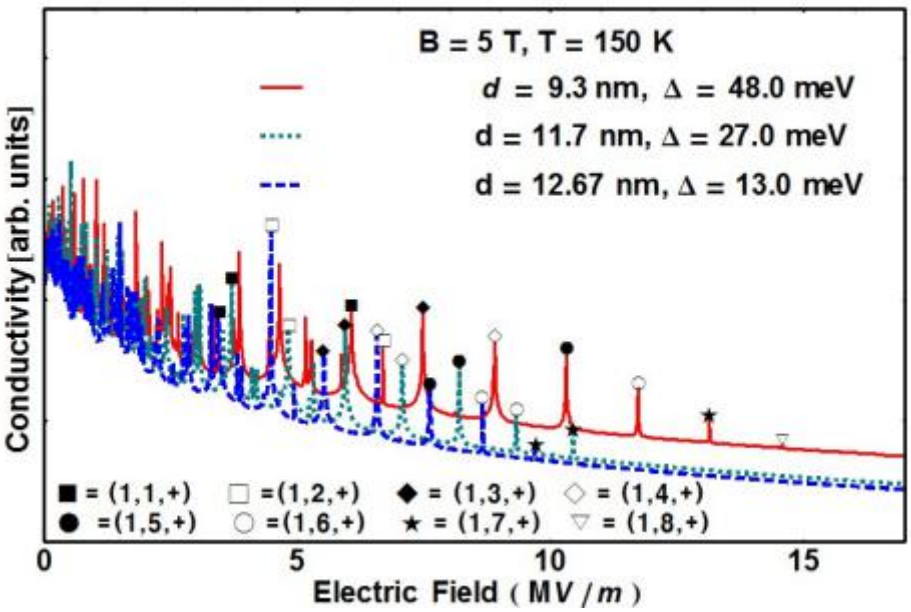

Fig. 6. Electric conductivity σ_{zz} as a function of the electric field for various periods and miniband widths in semiconductor superlattices at $B = 5\ T$ and $T = 150$ K. The solid, dotted, and dashed lines are for $d = 9.3$ nm ($\Delta = 48.0$ meV), $d = 11.7$ nm ($\Delta = 27.0$ meV) and $d = 12.6$ nm ($\Delta = 13.0$ meV), respectively [56].

An investigation is conducted on hopping conduction between localized Stark states in superlattices under longitudinal electric and magnetic fields. Consideration is given to electron scattering with polar-optic phonons, short-range impurities, and acoustic phonons [57]. The expression for hopping current formally exhibits a series of maxima at the points $p\omega_c = n\theta$ [Stark-cyclotron resonance (SCR)] or at $p\omega_c = n\theta \pm \omega_{0l}$ [Stark-cyclotron-phonon resonance (SCPR)]

(ω_c and θ are cyclotron and Bloch frequencies, respectively, ω_{0l} vol are optic-phonon frequency modes in superlattices, and p and n are integer numbers). However, because of finite collisional widening, the SCRs are substantially suppressed and difficult to detect experimentally. Numerical simulations conducted inside the dielectric continium model reveal that the amplitude of SCPR is far smaller than that of SCR and does not contribute to the hopping current. These findings are qualitatively consistent with recent research.

Bloch states are used to realize conduction along the field, and the momentum representation (miniband transport regime) is the basis for the description of transport in several formalisms [58–62]. In this instance, conduction is achieved through the hopping between localized "Stark states," and the Stark representation (hopping regime) provides an advantageous way to characterize it [63–65].

An interesting example is the variably spaced semiconductor superlattice (VSSL), which is designed to obtain a resonant tunneling between adjacent quantum-well states at a specific value of the growth-direction applied electric field. Such a heterostructure

was originally proposed by Summers and Brennan [66] to provide high-energy injection of electrons into a bulk semiconductor substrate at the operating bias and was thoroughly investigated from both theoretical [67–70] and experimental [71–73] points of view. Of special interest is the application of resonant heterostructures in photo-voltaic power generation. In that respect, Barnham and Duggan [74] proposed the use of a VSSL within a *p-i-n* structure to minimize the electron–hole recombination. More recently, Courel et al. [75,76] theoretically investigated the conversion efficiency of *p-i-n* GaAs/$Ga_{1x}In_xN_yAs_{1y}$ solar cells based on resonant tunneling and an improvement of 4% was achieved with respect to standard MQW solar cells. Similar studies in p-i-n GaAs/$Ga_{1x}In_xN_yAs_{1y}$ MQW solar cells were theoretically [77, 78] and experimentally [79] performed. The combined effect of applied electric and magnetic fields has proven to be a powerful tool in the study of several phenomena related to vertical transport in semiconductor heterostructures. Investigations of the influence of in-plane magnetic fields on the negative differential conductivity of double-barrier resonant heterostructures [80] and miniband transport in semiconductor superlattices under magnetic fields [81,82] were carried out at the end of the past century. Nowadays similar studies are of great importance in fields such as laser physics [83,84] and spintronics [85], to mention some few examples. In most of these studies of magnetic-field effects on the electrical and optical properties of resonant heterostructures, one observed a dramatic change in the photoluminescence (PL) spectrum as a function of the applied magnetic field. Similar results for the intraband absorption coefficient of VSSLs under crossed electric and magnetic fields were recently reported [86].

The interband optical absorption spectra of a GaAs/$Ga_{1-x}Al_xAs$ variably spaced semiconductor super-lattice under crossed in-plane magnetic and growth-direction applied electric fields are theoretically investigated. The electronic structure, transition strengths and interband absorption coefficients are analyzed within the weak and strong magnetic-field regimes. A dramatic quenching of the absorption coefficient is observed, in the weak magnetic-field regime, as the applied electric field is increased, in good agreement with previous experimental measurements performed in a similar system under growth-direction applied electric fields. A decrease of the resonant tunneling in the superlattice is also theoretically obtained in the strong magnetic-field regime. Moreover, in this case, we found an interband absorption coefficient weakly dependent on the applied electric field. Present theoretical results suggest that an in-plane magnetic field may be used to tune the optical properties of variably spaced semi-conductor superlattices, with possible future applications in solar cells and magneto-optical devices [87].

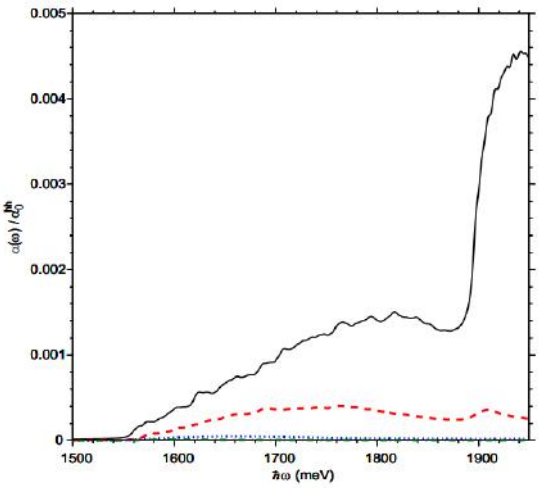

Fig.7. Total interband absorption coefficient as a functions of the photon energy $\hbar\omega$ in the GaAs–$Ga_{0.7}Al_{0.3}As$ variably spaced semiconductor superlattice for B=3 T and different values of the applied electric field. Solid, dashed, dotted, and dot-dashed lines correspond to applied electric fields F=0, F=10 kV/cm, F=20 kV/cm, and F=25 kV/cm, respectively [87].

A theory that considers the electron-phonon interaction in semiconductor superlattices under a magnetic field is proposed for the absorption of light by free charge carriers. The oscillations of the coefficient of light absorption by free charge carriers in the case of scattering by polar phonons were determined, depending on the resonance condition, the frequency of the incident light, and the magnetic field induction, within the framework of the second-order excitation theory, when the magnetic field is directed perpendicular to the surface of the semiconductor superlattice [88].

Density functional theory simulations were utilized to investigate the impact of stacking periodicity on the electrical and optical properties of the GaAs/AlAs superlattice [89]. The observation of the magnetic quantum ratchet effect in graphene with a lateral dual-grating top gate superlattice was reported [90]. In [91], the electrical and optical characteristics of the InAs/$InAs_{0.625}Sb_{0.375}$ superlattices were computed using the relativistic density functional theory paradigm.

[1] *A. Wacker.* Semiconductor superlattices: a model system for nonlinear transport. Phys. Rep. 357, 1-111, 2002.

[2] *A.Y. Shik*. Sov. Current-voltage characteristic of a narrow-band semiconductor taking account into ionization impurities. Phys. Semicond. 8, 1195,1975.

[3] *L. Esaki, R. Tsu.* Superlattice and negative differential conductivity in semiconductors. IBM J. Res. Develop. 14, 61, 1970.

[4] *A.Ya. Shik.* Superlattices-periodic semiconductor structures. FTP,1974, t.8, № 10, s. 1841-1864

[5] *E. Schomburg, J. Grenzer, K. Hofbeck, T. Blomeier, S. Winnerl, S. Brandl, A.A. Ignatov, K.F. Renk, D.G. Pavel'ev, Y. Koschurinov, V. Ustinov, A. Zhukov, A.Kovsch, S. Ivanov, P.S. Kop'ev.* Ultrafast creation and annihilation of space-charge domains in a semiconductor superlattice observed by use of Terahertz fields. Solid-State Electronics 42 1495, 1998.

[6] *Y. Shimada, K. Hirakawa, M. Odnoblioudov, and K. A. Chao.* Terahertz Conductivity and Possible Bloch Gain in Semiconductor Superlattices. Phys. Rev. Lett. 90, 046806, 2003.

[7] *P.G. Savvidis, B. Kolasa, G. Lee and S.J. Allen.* Resonant Crossover of Terahertz Loss to the Gain of a Bloch Oscillating InAs/AlSb superlattice. Phys. Rev. Lett. 92, 196802, 2004.

[8] *E. Schöll.* Nonlinear spatio-temporal dynamics and chaos in semiconductors (Cambridge University Press, Cambridge, 2001). Nonlinear Science Series, Vol. 10.

[9] *L.L. Bonilla and H.T. Grahn.* Non-linear dynamics of semiconductor superlattices. Rep. Prog. Phys. 68, 577, 2005.

[10] *Y. Zhang, J. Kastrup, R. Klann, K.H. Ploog and H.T. Grahn.* Synchronization and Chaos Induced by Resonant Tunneling in GaAs/AlAs Superlattices. Phys. Rev. Lett. 77, 3001,1996.

[11] *K.N. Alekseev, G.P. Berman, D.K. Campbell, E.H. Cannon and M.C. Cargo.* Dissipative chaos in semiconductor superlattices. Phys. Rev. B 54, 10625, 1996.

[12] *A. Amann, J. Schlesner, A. Wacker and E. Schöll.* Chaotic front dynamics in semiconductor superlattices. Phys. Rev. B 65, 193313, 2002.

[13] *T.M. Fromhold, A.A. Krokhin, C.R.. Tench, S. Bujkiewicz, P.B. Wilkinson, F.W. Sheard and L.Eave.* Effects of Stochastic Webs on Chaotic Electron Transport in Semiconductor Superlattices. Phys. Rev. Lett. 87, 046803, 2001.

[14] *T.M. Fromhold, A.Patanè, S.Bujkievicz, P.B.Wilkinson, D.Powler, D.Sherwood, S.P.Stapleton, A.A.Krokhin, L.Eaves, M. Henini, N.S. Sankeshwar and F.W. Sheard.* Chaotic electron diffusion through stochastic web enhances current flow in superlattices. Nature 428, 726, 2004.

[15] *D.P.A. Hardwick, S.L. Naylor, S. Bujkiewicz, T.M. Fromhold, D. Fowler, A. Patanè, L. Eaves, A.A. Krokhin, P.B. Wilkinson, M. Henini and F.W. Sheard.* Effect of interminiband tunneling on current resonances due to the formation of stochastic conduction networks in superlattices. Physica E 32, 285, 2006.

[16] *Y.A. Kosevich, A.B. Hummel, H.G. Roskos, and K. Köhler.* Ultrafast Fiske effect in semiconductor superlattices. Phys. Rev. Lett. 96, 137403, 2006.

[17] *R.Z. Sagdeev, D.A. Usikov and G.M. Zaslavsky*. Deterministic Chaos of Exponential Oscillons and Pulsons, Nonlinear Physics (Harwood Academic Publishers, NY, 1988).

[18] *G.M. Zaslavsky, R.Z. Sagdeev, D.A. Usikov, A.A. Chernikov.* Weak Chaos and Quasi-Regular Patterns. Cambridge University Press, Cambridge, 1991.

[19] *A.A. Vasiliev, G.M. Zaslavsky, M.Y. Natenzon, A.I. Neishtadt, B.A. Petrovichev, R.Z. Sagdeev, A.A. Chernikov.* Attractors and stochastic attractors of motion in a magnetic field. Sov. Phys. JETP 67, 2053, 1989. Zh. Eksp. Teor. Fiz. 94, 170, 1988.

[20] *S.P. Stapleton, S. Bujkiewicz, T.M. Fromhold, P.B. Wilkinson, A. Patan`e, L. Eaves, A.A. Krokhin, M. Henini, N.S. Sankeshwar and F.W.Sheard.* Use of stochastic web patterns to control electron transport in semiconductor superlattices. Physica D 199, 166, 2004.

[21] *A.G. Balanov, D. Fowler, A. Patan`e, L. Eaves and T.M. Fromhold.* Bifurcations and chaos in semiconductor superlattices with a tilted magnetic field.

[22] *V.L. Malevich and E.M. Epshtein*. Photostimulated odd magnetoresistance of semiconductors. Sov. Phys. Solid State (Fiz. Tverd. Tela) 18, 1976, 1286.

[23] *G.M. Shmelev, A.V. Yudina, I. I. Maglevanny and A.S. Bulygin.* Electric-field-induced Ettingshausen in a superlattice. Phys. Stat. Sol.(b) 219, 2000, 115.

[24] *Dao Thu Hang, Nguyen Vu Nhan and Nguyen Quang Bau*. Theoretical Study of the Magneto-Thermoelectric Effect in Doped Semiconductor Superlattices under the Influence of an Electromagnetic Wave by Using a Quantum Kinetic Equation Key Engineering Materials. Vol. 783, pp 93-102.

[25] *Dong Shik Kang, Suck, Whan Kim, Sang Chil Lee.* Orbital Magnetization and Heat Capacity in Bulk Semiconductor Superlattices under a Tilted Magnetic Field. New Physics: Sae Mulli (The Korean Physical Society), vol. 61, № 5, 2011.

[26] *Nguyen Quang Bau , Do Tuan Long*. Impact of confined LO-phonons on the Hall effect in doped semiconductor superlattices Journal of Science: Advanced Materials and Devices Volume 1, Issue 2, June 2016, Pages 209-213

[27] *D.Z. Mowbray, M. Cardona, K. Ploog*. Confined LO phonons in GaAs/AlAs superlattices. Phys. Rev. B 43, 1991, 1598e1603.

[28] *J.S. Bhat, B.G. Mulimani, S.S. Kubakaddi.* Electron-confined LO phonon scattering rates in GaAs/AlAs quantum wells in the presence of a quantizing magnetic field. Semicond. Sci. Technol. 8, 1993, 1571e1574.

[29] *N.Q. Bau, D.M. Hung, L.T. Hung*. The influences of confined phonons on the nonlinear absorption coefficient of a strong electromagnetic wave by confined electrons in doping superlattices. Prog. Electromagn. Res. Lett. 15, 2010, 175e185.

[30] *A.M. Paula, G. Weber.* Carrier capture processes in semiconductor superlattices due to emission of confined phonons. J. Appl. Phys. 77, 1995, 6306e6312.

[31] *A. Fasolino, E. Molinari, J.C. Maan.* Resonant quasiconfined optical phonons in semiconductor superlattices. Phys. Rev. B 39, 1989, 3923e3926.

[32] *P.Y. Yu, M. Cardona.* Fundamentals of Semiconductors. Springer Berlin, Heidelberg, 2005, pp. 469e551.

[33] *S. Rudin, T. Reinecke.* Electron-LO-phonon scattering rates in semiconductor quantum wells. Phys. Rev. B 41, 1990, 7713e7717.

[34] *N.Q. Bau, B.D. Hoi.* Dependence of the Hall coefficient on doping concentration in doped semiconductor superlattices with a perpendicular magnetic field. Integrated Ferroelectrics Số 1, năm 2014 (Tập 155, trang 39-44)

[35] *Sang Chil Lee and Dong Shik Kang , Jeong Dae Ko, Young Hun Yu and Jai Yon Ryu, Suck Whan Kim.* Magnetophonon Resonances in the Miniband Transport in Semiconductor Superlattices. Journal of the Korean Physical Society, Vol. 39, No. 4, October 2001, pp. 643- 654.

[36] *M.A. Brummell, D.R. Leadley, R.J. Nicholas, M.A. Hopkins, J.J. Harris and C.T. Foxon.* Modification of the Electron-Phonon Interactions in GaAs-GaAlAs Heterojunctions.Phys. Rev. Lett. 58, 77, 1988.

[37] *W. Xu, F. M. Peeters, J. T. Devreese, D. R. Leadley and R. J. Nicholas, Int. J. Mod.* Destruction of magnetophonon resonance in high magnetic fields from impurity and phonon scattering in heterojunctions. Phys. B 10, 169, 1996.

[38] *S. C. Lee, J. Y. Ryu, S. W. Kim and C. S. Ting.* Magnetization and magnetic susceptibility in a quantum-dot superlattice at low temperature. Phys. Rev. B 62, 5045, 2000.

[39] *H. Noguchi, H. Sakaki, T. Takamasu and N.Miura.* Observation of magnetophonon resonance in the miniband transport in semiconductor superlattices. Phys. Rev. B 45, 12148 (1992).

[40] *W.M. Shu and X.L. Lei.* Miniband transport in semiconductor superlattices in a quantized magnetic field. Phys. Rev. B 50, 17378, 1994.

[41] *P. Gassot, J. Genoe, D. K. Maude, J. C. Portal, K. S. H. Dalton, D. M. Symons, R. J. Nicholas, F. Aristone, J. F. Palmier and F. Laruelle.* Magnetophonons in short-period superlattices. Phys. Rev. B 54, 14540, 1996.

[42] *V.L. Gurevich, Yu.A. Firsov.* Zh. Eksp. Teor. Fiz. 40, 1961, 198, Sov. Phys. JETP 13, 1961, 137.

[43] *P. Vasilopoulos.* Magnetophonon oscillations in quasi-two-dimensional quantum wells. Phys. Rev. B 33, 1986, 8587.

[44] *N. Mori, K. Taniguchi, C. Hamaguchi, S. Sasa, S. Hiyamizu.* Magnetophonon resonance of a two dimensional electron gas in a quantum well. J. Phys. C 21, 1988, 1791.

[45] *A. Suzuki.* Theory of hot-electron magnetophonon resonance in quasi-two-dimensional quantum-well structures. Phys. Rev. B 45, 1992, 6731.

[46] *P. Vasilopoulos, P. Warmenbol, F.M. Peeters, J.T. Devreese.* Magnetophonon resonances in quasi-one-dimensional wires. Phys.Rev. B 40, 1989, 1810.

[47] *N. Mori, H. Momose, C. Hamaguchi.* Magnetophonon resonances in quantum wires. Phys. Rev. B 45, 1992, 4536.

[48] *J.Y. Ryu, R.F. O'Connell.* Magnetophonon resonances in quasi-one-dimensional quantum wires. Phys. Rev. B 48, 1993, 9126.

[49] *J.Y. Ryu, G.Y. Hu, R.F. O'Connell.* Magnetophonon resonances of quantum wires in tilted magnetic fields. Phys. Rev. 49, 1994, 10437.

[50] *J.P. Vasilopoulos, M. Charbonneau, C.M. Van Vliet.* Linear and nonlinear electrical conduction in quasi-two-dimensional quantum wells, Phys. Rev. B 35, 1987, 1334.

[51] *A. Suzuki, M. Ogawa.* Magnetophonon resonance of quasi-two-dimensional and quasi-one-dimensional electronic systems in tilted magnetic fields. J. Phys. C 10, 1998, 4659.

[52] *H. Noguchi, H. Sakaki, T. Takamasu, N. Miura.* Observation of magnetophonon resonance in the miniband transport in semiconductor superlattices. Phys. Rev. B 45 (1992) 12148.

[53] *W.M. Shu, X.L. Lei.* Miniband transport in semiconductor superlattices in a quantized magnetic field. Phys. Rev. B 50, 1994, 17378.

[54] *X.L. Lei, N.J.M. Horing, H.L. Cui.* Theory of negative differential conductivity in a superlattice miniband. Phys. Rev. Lett. 66, 1991, 3277.

[55] *Sang Chil Leea, Jeong Woo Kanga, Dong Shik Kanga, Young Bong Kanga, Kyung Hwa Kimb,Hyung Soo Ahnb, Min Yangb, Nam Lyong Kangc, Suck Whan Kimd.* Angular dependence of magnetophonon resonances in semiconductor superlattices in tilted magnetic fields. Physica B 387, 2007, 313–322.

[56] *Sang Chil Lee, Hyung Soo Ahn, Suck Whan Kim.* Wannier-Stark Mangnetophonon Resonance in Semiconductor Superlattices New Physics: Sae Mulli, Vol. 66, № 11, November 2016, pp. 1359~1365

[57] *Nguyen Hong Shon and H.N. Nazareno.* Hopping conduction in semiconductor superlattices in a quantized magnetic field.Physical Review b, volume 53, number 12, 1996.

[58] *A.Ya. Shik.* Fiz. Tekh. Poluprovodn. 7, 261, 1973. [Sov. Phys. Semicond. 7, 187 1973)].

[59] *R.A. Suris and B.S. Shchamkhalova.* Heating of electrons in superlattice semiconductors. Fiz. Tekh. Poluprovodn. 18, 1178, 1984, [Sov. Phys. Semicond. 18, 738, 1984].

[60] *Kazarinov and R.A. Suris.* Electric and electromagnetic properties of semiconductors with a superlattice, Fiz. Tekh. Poluprovodn. 6, 148, 1972, Sov. Phys. Semicond. 6, 120,1972.

[61] *Nguyen Hong Shon and H.N. Nazareno.* Influence of quantum-interference effects on hole mobility in superlattices, Rev. B 50, 8577 1994.

[62] *S.R. Eric Yang and S. Das Sarma*. Theory of conductivity in superlattice minibands. Phys. Rev. B 37, 10 090, 1988.

[63] *R. Tsu and G. Do ̈hler*. Phys. Rev. B 12, 680, 1975; *G.H. Döhler, R. Tsu, and L. Esaki*. Solid State Commun. 17, 317, 1975.

[64] *R. Tsu and L. Esaki*. Phys. Rev. B 43, 5204 1991.

[65] *Jian-Bai Xia*. Phys. Rev. B 50, 15 067, 1994.

[66] *C.J. Summers, K.F. Brennan.* Variably spaced superlattice energy filter, a new device design concept for high-energy electron injection. Appl. Phys. Lett. 48 (12), 1986, 806–808.

[67] *K.F. Brennan, C.J. Summers*. Theory of resonant tunneling in a variably spaced multiquantum well structure: an Airy function approach. J. Appl. Phys. 61 (2), 1987, 614–623.

[68] *K.F. Brennan, C.J. Summers.* The variably spaced superlattice electroluminescent display: a new high efficiency electroluminescence scheme. J. Appl. Phys. 61 (12), 1987, 5410–5418.

[69] *C.J. Summers, K.F. Brennan*. New resonant tunneling superlattice avalanche photodiode device structure for long-wavelength infrared detection. Appl. Phys. Lett. 51 (4), 1987, 276–278.

[70] *S.M. Cao, M. Willander, E.L. Ivchenko, A.I. Nesvizhskii, A.A. Toropov*. Electrons and excitons in an imperfect superlattice in electric fields. Superlatt. Micro-struct. 17 (1), 1995, 97–105.

[71] *S.M. Cao, M. Willander, A.A. Toropov, T.V. Shubina, B.Y. Mel'tser, S.V. Shaposhnikov, P.S. Kop'ev, P.O. Holtz, J.P. Bergman, B. Monemar*. Resonant coupling of electrons and excitons in an aperiodic superlattice under electric fields studied by photoluminescence spectroscop. Phys. Rev. B 51, 1995, 17267–17270.

[72] *S.M. Cao, M. Willander, A.A. Toropov, T.V. Shubina, B.Y. Mel'tser, S. V. Shaposhnikov, P.S. Kop'ev, J.P. Bergman, P.O. Holtz, B. Monemar.* Characterization of $Al_{0.4}Ga_{0.6}As$/GaAs aperiodic superlattices by photoluminescence spectroscopy at 2 K. Superlatt. Microstruct. 20 (2), 1996, 229–235.

[73] *S.M. Cao, M. Willander, A.A. Toropov, T.V. Shubina, B.Y. Mel'tser, P.S. Kop'ev, T. Lundström, P.O. Holtz, J.P. Bergman, B. Monemar*. Bistable electroluminescence in p-i-n light-emitting tunnel-diodes enhanced by aperiodic-superlattice injectors. Appl. Phys. Lett. 72 (3), 1998, 347–349.

[74] *K.W.J. Barnham, G. Duggan.* A new approach to high efficiency multiband gap solar cells. J. Appl. Phys. 67 (7), 1990, 3490–3493.

[75] *M. Courel, J.C. Rimada, L. Hernánde.* GaAs/GaInNAs quantum well and superlattice solar cell. Appl. Phys. Lett. 100 (7), 2012, 073508.

[76] *M. Courel, J.C. Rimada, L. Hernández.* An approach to high efficiencies using GaAs/GaInNAs multiple quantum well and superlattice solar cell. J. Appl. Phys. 112 (5), 2012, 054511.

[77] *C.I. Cabrera, J.C. Rimada, M. Courel, L. Hernandez, J.P. Connolly, A. Enciso, D. A. Contreras-Solorio.* Modeling multiple quantum well and superlattice solar cells. Nat. Resour. 04 (03), 2013, 235–245.

[78] *C.I. Cabrera, J.C. Rimada, J.P. Connolly, L. Hernandez*. Modeling of GaAsP/In-GaAs/GaAs strain-balanced multiple-quantum well solar cells. J. Appl. Phys. 113 (2), 2013, 024512.

[79] *B. Royall, H. Khalil, S. Mazzucato, A. Erol, N. Balkan.* Experimental investigation and numerical modeling of photocurrent oscillations in lattice matched $Ga_{1x}In_xN_yAs_{1y}$/GaAs quantum well p-i-n photodiodes. Nanosc. Res. Lett. 9 (1), 2014, 84.

[80] *M.L. Leadbeater, L. Eaves, P.E. Simmonds, G.A. Toombs, F.W. Sheard, P.A. Claxton, G.Hill, M.A. Pate.* Magnetic-field studies of negative differential conductivity in double barrier resonant tunnelling structures based on n InP/ (InGa)As, Solid-State Electron. 31 (3–4), 1988, 707–710.

[81] *H.J. Hutchinson, A.W. Higgs, D.C. Herbert, G.W. Smith*. Observation of miniband transport in GaAs/$Al_{0.33}Ga_{0.67}As$ superlattices. J. Appl. Phys. 75 (1), 1994, 320–324.

[82] *W.M. Shu, X.L. Lei.* Miniband transport in semiconductor superlattices in a quantized magnetic field. Phys. Rev. B 50 (23), 1994, 17378–17382.

[83] *S. Blaser, L. Diehl, M. Beck, J. Faist.* Long-wavelength (λ~10.5 μm) quantum cascade lasers based on a photon-assisted tunneling transition in strong magnetic field. Physica E 7 (1–2), 2000, 33–36.

[84] *G.G. Zegrya, N.V. Tkach, I.V. Boiko, Y.A. Seti.* Quasi-stationary electron states in a multilayered structure in longitudinal electric and transverse magnetic fields. Phys. Solid State 55 (10), 2013, 2182–2189.

[85] *J. Silvano de Sousa, H. Detz, P. Klang, E.Gornik, G. Strasser, J. Smoliner.* Enhanced Rashba effect in transverse magnetic fields observed on InGaAs/ GaAsSb resonant tunneling diodes at temperatures up to T⁄4180 K. Appl. Phys. Lett. 99 (15), 2011, 152107.

[86] *E. Reyes-Gómez, N. Raigoza, L.E. Oliveira*. Intraband absorption in GaAs–(Ga,Al)As variably spaced semiconductor superlattices

under crossed electric and magnetic fields Europhys. Lett. 104 (4), 2013, 47008.

[87] *J.N. Zuleta, E. Reyes-Gómez.* Effects of crossed electric and magnetic fields on the interband optical absorption spectra of variably spaced semiconductor superlattices. Physica B: Condensed Matter Volume 488, 1 May 2016, Pages 72-82.

[88] *G.B. Ibragimova and R.Z. Ibaevaa*. Light Absorption by Free Charge Carriers with Scattering Mechanisms in a Semiconductor Superlattice. Journal of Surface Investigation: X-ray, Synchrotron and Neutron Techniques, 2024, Vol. 18, № 1, pp. 116–120.

[89] *M. Jiang, H. Y. Xiao, S. M. Peng, L. Qiao, G. X. Yang, Z. J. Liu, and X. T. Zu.* Effects of stacking periodicity on the electronic and optical properties of GaAs/AlAs superlattice: a first-principles study. Sci. Rep. 10, 4862, 2020.

[90] *S. Hubmann, V. V. Belkov, L. E. Golub, V. Yu. Kacho-rovskii, M. Drienovsky, J. Eroms, D. Weiss, and S. D. Ganichev.* Giant ratchet magneto-photocurrent in graphene lateral superlattices. Phys. Rev. Res. 2, 033186 (2020).

[91] *H. Ghulam, C. Giuseppe, I. Rajibul, T. Artur, J. Jarosław, A. Carmine, and D. Tomasz.* J. Phys. D. 55,495301, 2022.

Received: 10.07.2024

THERMOPHYSICAL, DIELECTRIC AND CONDUCTIVITY PROPERTIES OF PLASMA-MODIFIED COMPOSITES BASED ON PVDF DISPERSED WITH $BATIO_3$ PARTICLES

I.S. RAMAZANOVA, G.Kh. GUSEYNOVA, U.V. YUSIFOVA, T.D. IBRAGIMOV, A.F. NURALIYEV, F.F. YAHYAYEV

Institute of Physics, Ministry of Science and Education of Azerbaijan, H. Javid ave. 131, Baku, AZ 1143

irada-sultanakhmedova@rambler.ru

The effect of barrier electric discharge plasma on thermophysical, dielectric and conductive properties of PVDF+$BaTiO_3$ based composite has been studied. It is shown that the enthalpy and entropy of melting and solidification decrease sharply when the filler is included, and a relative increase is observed at a concentration of 20%. At the other concentrations, however, except at 10% and 30%, these physical quantities decrease after exposure to barrier electric discharge plasma. This increase is negligible for pure polyvinylidene fluoride but significant for composites. Also the dielectric permittivity increases with increasing concentration. It is shown that the conductivity first increases with increasing filler concentration, reaches a maximum at 20% concentration and then decreases. After exposure to barrier electric discharge plasma, the dielectric permittivity and conductivity decrease.

Key words: barium titanate, polyvinylidene fluoride, dielectric permittivity; electric conductivity, composite material.
PACS: 77.55.+f , 77.84._s , 77.84.Dy, 77.84.Lf, 81.07.Pr , 82.35.Np

INTRODUCTION

Polymer-inorganic composite materials with high dielectric constant and low losses, combining viscoelastic properties of the polymer with dielectric properties of the filler, are necessary for the creation of numerous devices. One of the most promising materials of this type are composites based on a segmentoelectric filler - barium titanate. The review article [1] presents data on the permeability of ceramics based on barium titanate with different grain sizes. In this work, the influence of calcined barium titanate powders on the electrical properties of barium titanate/polyvinylidene fluoride composites is investigated. The crystal structure of $BaTiO_3$ powders, piezoelectric and dielectric properties of barium titanate/polyvinylidene fluoride composites were systematised. The results showed that the appropriate calcination temperature of barium titanate fillers could improve the electrical properties of the composites. When barium titanate powders were calcined at 950 0C, the dielectric constant εr and piezoelectric strain constant d33 of barium titanate/polyvinylidene fluoride composites reached the maximum values of 166.38 and 25 pKl/N, respectively, while the dielectric loss tan δ was maintained [2]. The frequency and temperature dependences of dielectric permittivity and electrical conductivity of high-density polyethylene with the addition of monodisperse barium titanate particles were studied. It is shown that dielectric permittivity and electrical conductivity increase with increasing filler concentration at all temperatures. In this case, the conductivity has a hopping mechanism described by the Josher theory. The corresponding parameter of degree index and activation energy decrease with increasing concentration of barium titanate [3].

Electrodischarge plasma modification is one of the most efficient methods compared to other methods requiring vacuum conditions. In the process of electro-discharge plasma treatment, a process of functionalisation takes place on the polymer surface with the formation of various polar groups containing oxygen [4, 5]. Various forms of plasma, including corona discharge plasma [6], barrier discharge plasma [7, 8] and low pressure O_2 glow discharge plasma [6], have been used to modify the properties of low density polyethylene film. The results obtained indicate good processing uniformity and improved adhesion properties after these processes. The authors of [9] showed that the electric discharge plasma process leads to the formation of deep traps with high concentration in the electret composite and reduces the probability of local centre ionisation during electrothermopolarisation. In [10], porous polyethylene films were treated with dielectric surface-barrier discharge plasma at atmospheric pressure in oxygen or nitrogen, as well as radio frequency discharge plasma. A noticeable increase in the surface energy and polar component of porous polyethylene films modified by all types of plasma was found. In [11], plasma treatment of coated and uncoated polymer films and particles by plasma is considered. The authors suggest that the threefold difference in the processing rate of films in ammonia plasma is a consequence of their quasi-crystalline structure compared to amorphous polyethylene films. In [12], high density polyethylene (HDPE) with semiconducting or dielectric fillers was prepared by hot pressing method. The results showed that an increase in filler concentration is accompanied by a corresponding increase in thermal conductivity. In [13], the crystallisation of "polymer-segnetoelectric/piezoceramic" composites under the action of electric discharge plasma and temperature was investigated. It is shown that this process leads to strong oxidation of polymer chains. Thus, the method of plasma modification of polymers and composites based on them can find a wide practical application.

131, H.Javid ave, AZ-1143, Baku
Institute of Physics
E-mail: jophphysics@gmail.com

The practical application of composites requires a fundamental understanding of the interaction properties between the components. One of the most promising materials are composites based on segmentoelectric barium titanate as a filler. Its particles increase the dielectric constant and electrical conductivity of the polymer [14] and form local electric fields in liquid crystals, improving the switching time [15-19].

The present work focuses on the electrical and dielectric properties of composites before and after plasma treatment.

The present report is devoted to the effect of barrier discharge plasma on the thermophysical, dielectric and electrical conductive properties of PVDF-$BaTiO_3$ composites.

2. MATERIALS AND METHODS

Polyvinylidene fluoride (PVDF) was used as a matrix. The melting and softening temperatures of the polymers are 170-175°C and 140-160°C, respectively. Barium titanate particles of 600 nm (USA, Research Nanomaterials, In.) were added to the fine powder of polyvinylidene fluoride at different concentrations (5 vol%, 10 vol%, 20 vol% and 30 vol%.)).

The resulting mixture was shaken in a vortex mixer for 1 hour at room temperature followed by ultrasonic treatment with a NATO CD-4800 Ultrasonic Cleaner (China) for 4 hours. Disc-shaped composite samples were obtained by hot pressing at 165°C and 15 MPa pressure. The pressing time after reaching the selected temperature is 15-20 minutes. The diameter and thickness of the obtained films were 4 cm and 80-90 μm, respectively. Aluminium electrodes with a diameter of 3 cm and a thickness of 10 μm were pressed on both sides of the films.

Nonthermal non-equilibrium plasma, called surface microdischarges (SMD), has been used as electrical discharges. SMD generation at atmospheric pressure is achieved using dielectric barrier discharge (DBD) technology, which belongs to the corona discharge family. In this case, the electric charge voltage in the cells is 8 kV.

A differential scanning calorimeter DSC 204 F1 (Netzsch, Germany) with a CC200 F1 liquid nitrogen flow-controlled cooling system was used to determine the thermophysical parameters. Argon at 50 kPa was used to purge and protect the cell. DSC204F1 and Proteus Analysis software were used to process the results. The rate of temperature change was 10 deg/min over the temperature range from 200°C to 1500°C. The exposure time was 30 min.

The critical temperature Tcr, at which the composite transitions from one state to another, was determined by the local maximum of heat flux, and the enthalpy change ΔH was determined by the expression:

$$\Delta H = k \cdot \Delta A, \quad (1)$$

where k is characteristic for the given device, A is the area under the corresponding peak. The entropy change ΔS during the transition was determined as:

$$\Delta S = \frac{\Delta H}{T_{cr}}. \quad (2)$$

The degree of crystallinity K was found by the expression:

$$K = \frac{\left|\Delta H_h + \Delta H_c\right|}{\Delta H(100\% cryst)} 100\% \quad (3)$$

where ΔH_h and ΔH_c are enthalpy changes at heating and cooling, respectively; ΔH (100% crystal) is enthalpy change at 100% crystallisation of the matrix. For polyvinylidene fluoride, the enthalpy change at 100% crystallisation was assumed to be 105 J/g.

Dielectric measurements were performed using a Precision LCR Meter 1920 (IET Labs. Inc., USA) in the frequency range of 20 Hz to 1 MHz and at 18°C to 70°C. The applied voltage was 0.5 V. The values of dielectric constant ε were determined as follows

$$\varepsilon = \frac{Cd}{\varepsilon_0 S}, \quad (4)$$

where ε_0 is the dielectric constant of free space, d and S are the thickness and area of the sample, respectively. The real ε' and figurative ε'' parts of dielectric permittivity and electrical conductivity σ were calculated by expressions:

$$\varepsilon' = \frac{\varepsilon}{\sqrt{1+D^2}}, \quad (5)$$

$$\varepsilon'' = \frac{\varepsilon D}{\sqrt{1+D^2}}, \quad (6)$$

$$\sigma = 2\pi f \varepsilon_o \varepsilon'', \quad (7)$$

3. RESULTS AND DISCUSSION

Figure 1 shows typical dependences of heat flow on temperature (DSC curves). Similar curves are observed for other filler concentrations.

As can be seen, the critical temperature during cooling process is observed at lower temperatures than the critical temperature during heating. This indicates that the composite crystallises at lower temperature. Moreover, the critical temperature decreases with increase in concentration and also after the action of barrier discharge. As the concentration of crystalline $BaTiO_3$ in the composite increases, the crystalline phase also increases. Since the phase transition of the crystalline structure occurs at a lower temperature compared to the amorphous phase, the increase of the crystalline phase also here causes a decrease in the phase transition temperature in the composite.

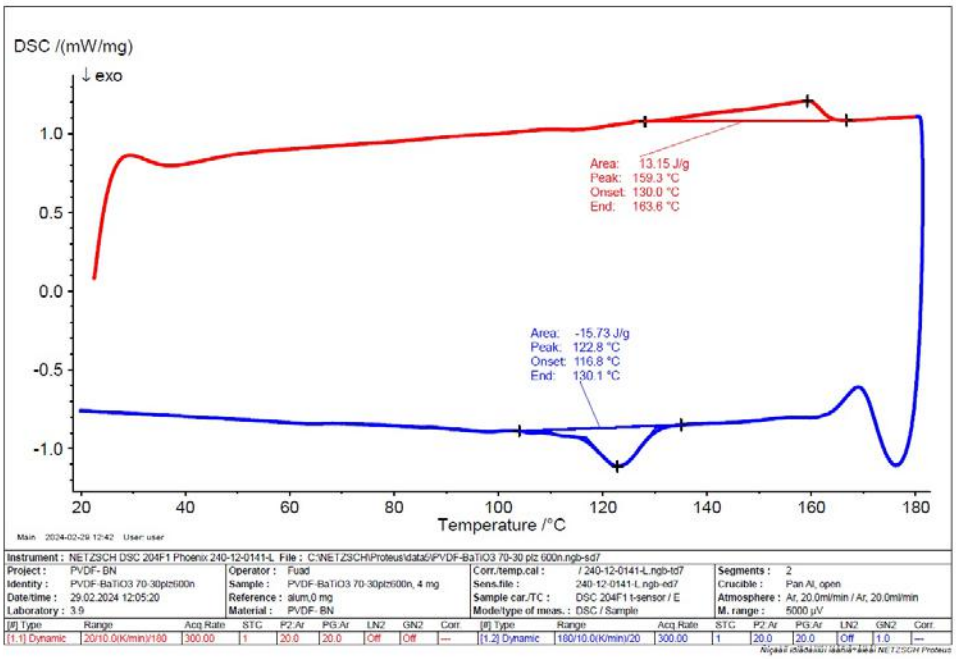

Fig.1. Temperature dependence of heat flow (DSC curves) for 70% PVDF+30% $BaTiO_3$ composite before and after plasma modification.

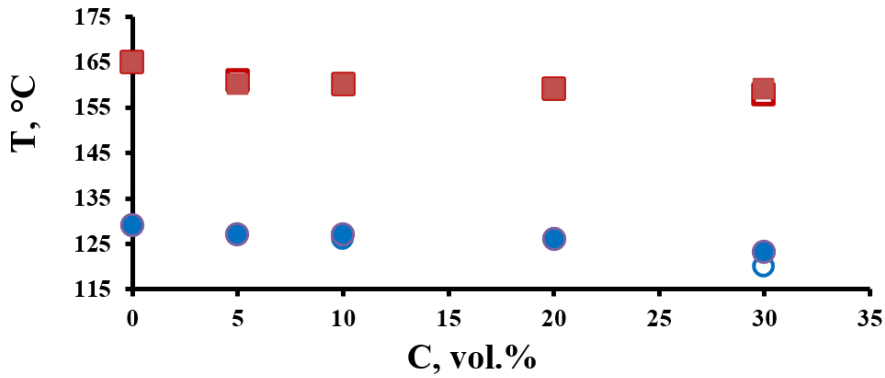

Fig. 2. Concentration dependence of the critical temperature of samples before and after the action of barrier discharge plasma. (empty circles) cooling regime before treatment, (filled circles) cooling regime after treatment; (empty squares) heating regime before treatment; (filled squares) heating regime after treatment.

Figure 2 shows the concentration dependence of the critical temperature of the samples before and after the discharge action.

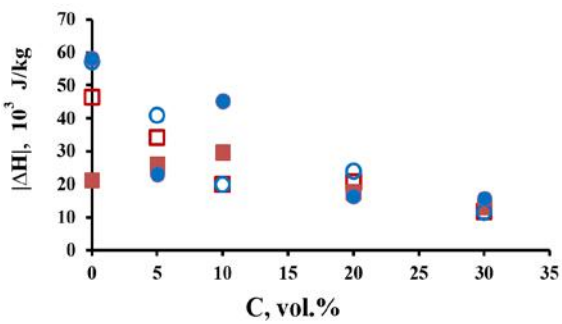

Fig. 3. The enthalpy change as a function of filler concentration: (empty circles) cooling regime before treatment; (filled circles) cooling regime after treatment; (empty squares) heating regime before treatment; (filled squares) heating regime after treatment.

Fig. 3 shows the dependence of the enthalpy of phase transition of samples before and after plasma at heating and cooling on the dispersant concentration. As can seen, with increasing filler concentration in the composite, the enthalpy before and after barrier discharge plasma during heating and cooling decreases. After barrier discharge plasma at heating and cooling processes enthalpy decreases at concentrations of 0, 5, 20% and enthalpy increases at concentrations of 10, 30%.

Fig. 4 shows the dependence of entropy of phase transition of samples on the filler concentration before and after plasma treatment at heating and cooling. As can see, the enthalpy of transition before and after the barrier discharge plasma during heating and cooling decreases with increasing filler concentration in the composite. Moreovere, during the barrier discharge plasma heating and cooling processes, the enthalpy of transition decreases at concentrations of 0, 5, 20% and enthalpy increases at concentrations of 10, 30%.

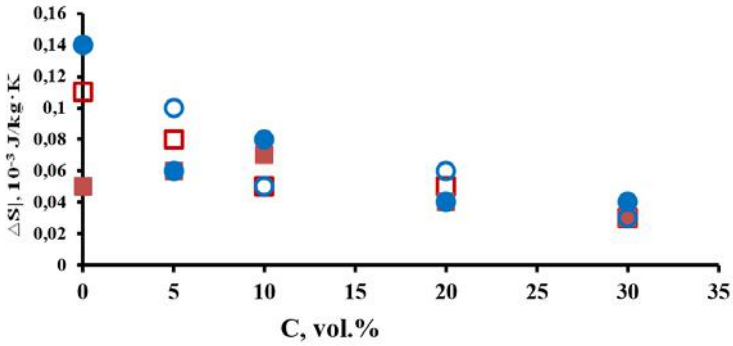

Fig. 4. Entropy change as a function of filler concentration: (empty circles) pre-treatment cooling mode, (filled circles) post-treatment cooling mode; (empty squares) pre-treatment heating mode; (filled squares) post-treatment heating mode.

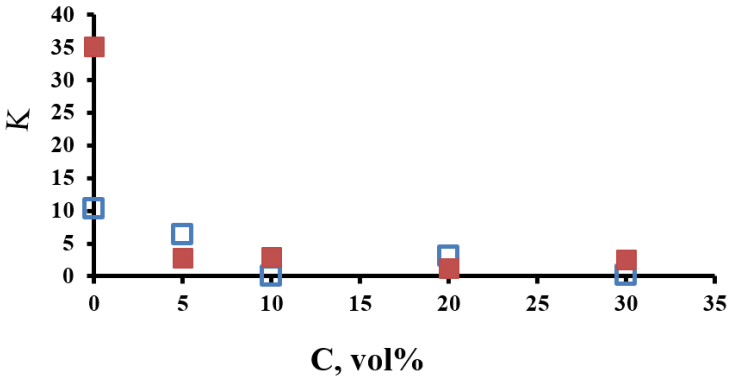

Fig.5. Dependence of crystallinity on dispersant concentration before and after the barrier electric discharge plasma. (empty squares) before treatment; (filled squares) after treatment.

Fig. 5 shows the dependence of the crystallinity on the filler concentration before and after the barrier discharge plasma. It can be seen from here that the crystallinity after plasma increases in pure polymer and composite at filler concentrations of 10 and 30% and decreases at concentrations of 5 and 20%.

The reason why the melting temperature of the polymer and composite is higher than the curing temperature is that the melting process requires the destruction of the ordered structure of the polymer chains, which is energetically more costly than the ordering or crystallisation process during cooling. As the polymer cools, its molecules lose energy and gradually begin to form into a more ordered structure, leading to solidification or crystallisation. This process requires less energy than melting to break down these structures and therefore occurs at a lower temperature.

It is known that the enthalpy of melting of a substance is the energy that is absorbed by the body in the form of heat during the transition from solid to liquid state, and for crystalline substances this occurs without increasing the temperature. It serves to disorganise the intermolecular bonds holding the molecules together. In solidification, the opposite process occurs when heat is removed from the substance. In this case, the intermolecular bonds are restored and the temperature does not change. For crystalline substances, the enthalpy change during melting and solidification has the same value. The degree of crystallinity of polymers is small, so the above laws do not apply to them. Enthalpy is an extensive quantity, i.e. for a composite system it is equal to the sum of enthalpies of its independent parts. Similarly, the enthalpy change of the composite is also the sum of the enthalpy changes of the matrix and filler. When the filler enters the polymer, the intermolecular bonds between individual groups of atoms shift. In particular, the chains in the macromolecule of the polymer are broken. As a result, less energy is required to completely disorganise the polymer chains, i.e. the enthalpy of fusion is significantly reduced. Further increase in the concentration of crystalline filler leads to a slight increase in enthalpy, as more energy is required to break the bonds in a larger volume of filler. A similar process occurs during solidification of the composite.

The entropy of melting and solidification is a measure of the disorder in the material accompanying melting or solidification, not only in the sense of changes in the arrangement of atoms and their configuration, but also in the sense of changes in the nature of chemical bonds. The higher value of the entropy of solidification compared to the entropy of melting is explained by the more ordered state of the composite in the solid phase during cooling. This is also consistent with the lower transition temperature. The entropy and enthalpy of transition are interrelated and their variation with concentration is explained in a similar manner.

These considerations agree well with the experimental curves of enthalpy and entropy change as a function of concentration. It is evident that the overall degree of crystallinity of composites increases with increasing volume of crystalline filler.

The barrier discharge plasma technique used modifies the composite not only on the surface but also in the volume [6, 7]. This type of discharge is accompanied by the formation of accelerated electrons and ions, recombination radiation, active gas products and the occurrence of surface electron-ion effects [11]. The process occurs as a result of polymer chain rupture, which allows such phenomena as cross-linking, free radical formation, etc. to occur, dramatically affecting the final characteristics of polymeric materials. The surface of composites can oxidise when exposed to oxygen environment. According to [14-15], as the concentration of oxygen atoms increases, additional oxidised species appear. In particular, ketone [-(C=O)-] and acetal [-(O-C-O)-] carbons are formed, and the latter is a carboxyl [-(C-O)-O-] carbon. The formation of new bonds favours the increase in the crystallinity of the composite. This is consistent with the experimental concentration-dependent crystallinity curves. At the same time, the decrease in the degree of crystallinity before and after treatment is due to the decrease in the volume fraction of polyethylene with increasing filler volume concentration.

The reason why the melting temperature of both polymer and composite is higher than its curing temperature is that the melting process requires the destruction of the ordered structure of the polymer chains, which is energetically more costly than the process of ordering or crystallisation on cooling. . As the polymer cools, its molecules lose energy and gradually begin to organise themselves into a more ordered structure, leading to solidification or crystallisation. This process requires less energy than melting to break down these structures, so it occurs at a lower temperature.

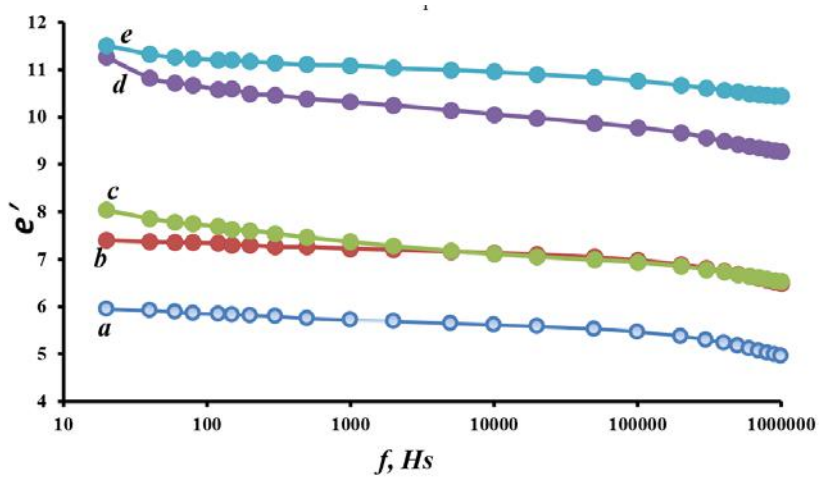

Fig. 6. Frequency dependences of real part of dielectric permittivity before treatment: (*a*) pure PVDF, (*b*) PVDF+ 5 vol.% filler, (*c*) PVDF+ 10 vol.% filler, (*d*) PVDF+ 20 vol.% filler, (*e*) PVDF+ 30 vol.% filler.

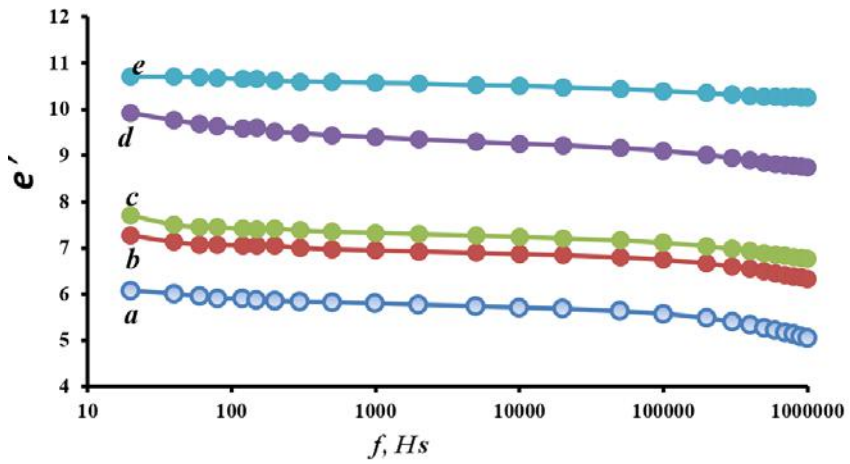

Fig. 7. Frequency dependences of real part of dielectric permittivity before treatment: (*a*) pure PVDF, (*b*) PVDF+5 vol.% filler, (*c*) PVDF+ 10 vol.% filler, (*d*) PVDF+ 20 vol.% filler, (*e*) PVDF+ 30 vol.% filler.

Figures 6 and 7 show frequency dependences of real parts of dielectric permittivity of samples before and after the action of barrier discharge. It can be seen from the figures that with increasing filler concentration the real part of dielectric permittivity of the samples increase. As the frequency increases, these values relatively decrease. As can be seen from this figure, the dielectric permittivity of the composites decrease with increase in frequency. Since the matrix we used is a polar dielectric, this change in the dielectric permittivity is due to the decrease in the number of polarized particles.

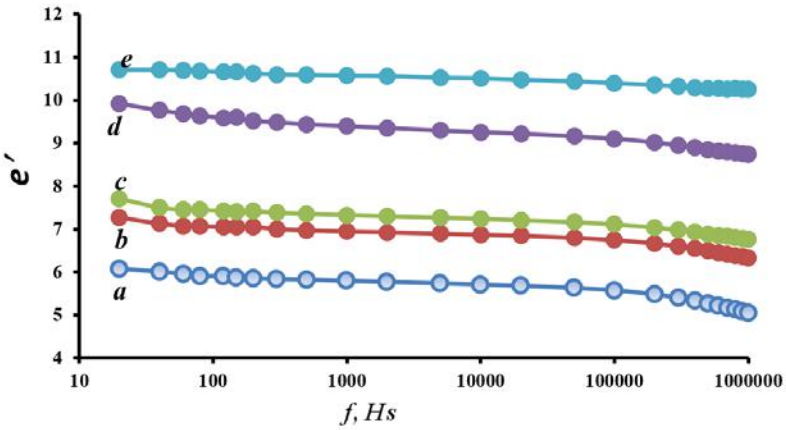

Fig. 8. Frequency dependences of real part of dielectric permittivity after treatment: (*a*) pure PVDF, (*b*) PVDF+ 5 vol.% filler, (*c*) PVDF+ 10 vol.% filler, (*d*) PVDF+ 20 vol.% filler, (*e*) PVDF+ 30 vol.% filler.

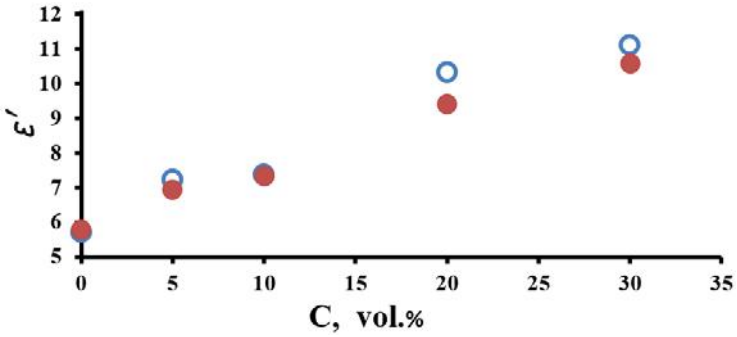

Fig. 9. Concentration dependence of real part of dielectric permittivity of samples before and after barrier discharge plasma at 1 kHz: (empty circles) before the discharge action, (filled circles) after the discharge action.

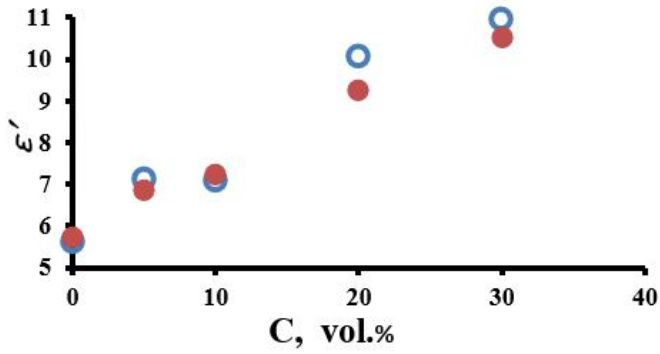

Fig. 10. Concentration dependence of real part of dielectric permittivity of samples before and after barrier discharge plasma at 10 kHz: (empty circles) before the discharge action, (filled circles) after the discharge action.

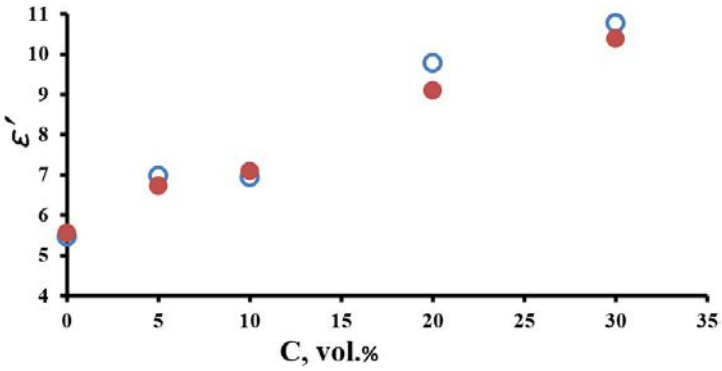

Fig. 11. Concentration dependence of real part of dielectric permittivity of samples before and after barrier discharge plasma at 100 kHz: (empty circles) before the discharge action, (filled circles) after the discharge action.

Figures 9-12 show the real parts of dielectric permittivity of samples before and after plasma treatment at 1 kHz, 10 kHz, 100 kHz and 1 MHz as a function of concentration. It can be seen from the figures that the dielectric constant increases after plasma in pure polymer. As the concentration of filler in the composite increases, the real value of dielectric constant after plasma decreases. When the pure polymer is exposed to plasma, oxygen-containing groups are formed in the air layer. Exposure of barrier electric discharge plasma leads to a decrease in dielectric permittivity of all samples, which is due to the change in the structure of the samples with the formation of new structural elements.

Figure 13 shows the frequency dependence of the conductivity of PVDF+10%$BaTiO_3$ composite before and after plasma. The figure shows that the conductivity decreases after plasma, and with increasing frequency the conductivity increases.

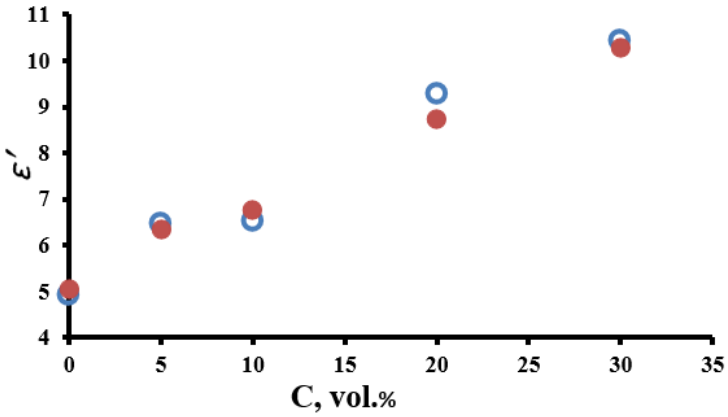

Fig.12. Concentration dependence of real part of dielectric permittivity of samples before and after barrier discharge plasma at 1 MHz: (empty circles) before the discharge action, (filled circles) after the discharge action.

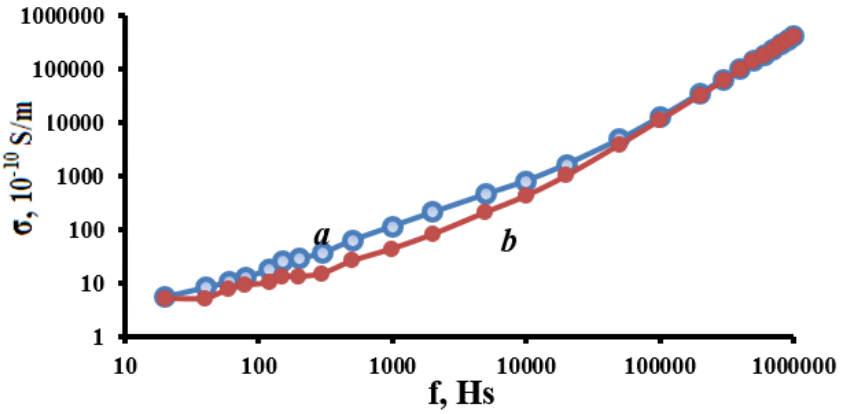

Fig. 13. Frequency dependence of the electric conductance for the composite with 10 vol.% filler: (*a*) before gas discharge treatment, (*b*) after gas discharge treatment.

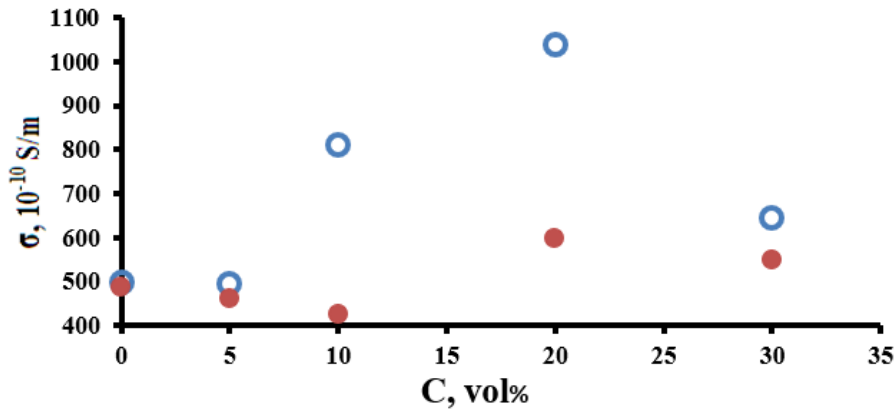

Fig. 14. Composite conductivity as a function of filler concentration at 10 kHz: (empty circles) before gas discharge treatment, (filled circles) after gas discharge treatment.

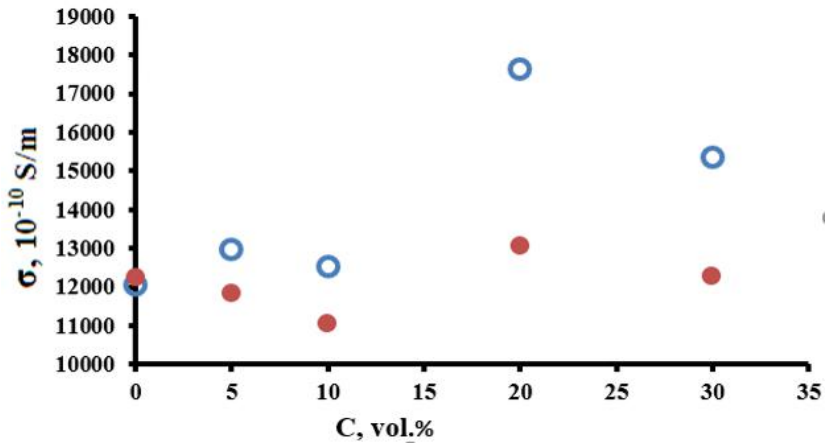

Fig. 15. Composite conductivity as a function of filler concentration at 100 kHz: (empty circles) before gas discharge treatment, (filled circles) after gas discharge treatment.

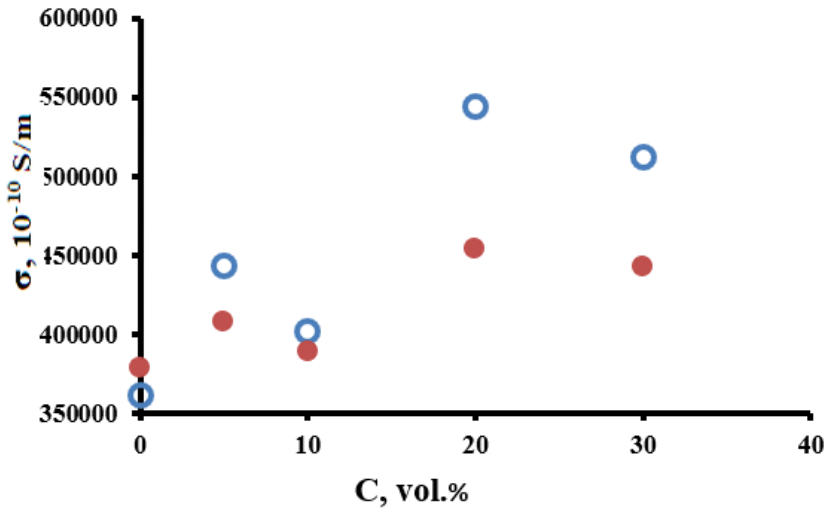

Fig. 16. Composite conductivity as a function of filler concentration at 1 MHz: (empty circles) before gas discharge treatment, (filled circles) after gas discharge treatment.

Figures 14-16 show the concentration dependences of the conductivity of samples before and after plasma at frequencies of 10 kHz, 100 kHz and 1 MHz. From here it can be seen that the conductivity of pure polymer decreases after barrier discharge plasma. As the dispersant concentration increases, the permeability decreases after the plasma. Also as the concentration of dispersant increases, the conductivity of samples before and after plasma first increases, reaches a maximum at 20% concentration and then decreases. When pure polymer is exposed to plasma, the crystalline phase of the polymer increases and the electrons of this phase contribute to the increase in conductivity. When exposed to barrier electric discharge plasma, the oxygen-containing groups formed in the air gap lead to the formation of new traps in the polymer phase [11-15]. These traps impede the movement of electrons and the conductivity decreases.

CONCLUSIONS

It has been found that when $BaTiO_3$ is added to PVDF, the enthalpy and entropy of the phase transition and the crystallinity decrease as the filler concentration increases. This is due to the increase in defectivity of the sample as the concentration increases and the thermal energy required for the transition from one phase state to another decreases. As the filler concentration increases before and after the plasma, the real part of dielectric permittivity of the samples increases, As the concentration of filler in the polymer matrix increases, the number of defects in the sample increases as well as after the action of the discharge. These defects act as traps for charge carriers. As a result, the conductivity decreases.

[1] *T.D. Ibragimov, I.S. Ramazanova, G.Kh. Guseynova, U.V. Yusifova, A.F. Nuraliyev.* Dielectric properties of polyethylene doped with barium titanate particles. AJP Fizika, 2022 28(1), pp.43-45.

[2] *Rui Li, Zhenhua Zhao, Zixuan Chen, and Jianzhong Pei.* Novel $BaTiO_3$/PVDF composites

with enhanced electrical properties modified by calcined $BaTiO_3$ ceramic powders. Mater. Express, Vol. 7, № 6, 2017, pp.536-540.

[3] *T.D. Ibragimov, I.S. Ramazanova, G.Kh. Guseynova, U.V. Yusifova, A.F. Nuraliyev.* Dielectric and conductivity properties of polyethylene doped with barium titanate particles. UNEC Journal of Engineering and Applied Sciences Vol. 2, № 1, 2022, pp. 5-12

[4] *Novak, M. Steviar, A. Popelka, I. Chodak, J.Mosnacek, M. Spırkova, I. Janigova, A.Kleinova, J. Sedliacik, M. Slouf.* Surface Modification of polyethylene by diffuse barrier discharge plasma. J. Polym. Engineering and Sci. 53 (3), 1, 2012, pp.

[5] *W. Kun, L. Jian, R. Chunsheng, W. Dezhen, W.Younian. Surface* modification of polyethylene (PE) films using dielectric barrier discharge plasma at atmospheric pressure. J. Plasma Sci. and Technol. 10 (4), 433, 2008.

[6] *J.M. Grace, L.J. Gerenser.* Plasma treatment of polymers, J. Dispersion Sci. Technol. 24, 305, 2003.

[7] *S. Guimond, M.R. Wertheimer*. Surface degradation and hydrophobic recovery of polyolefins treated by air corona and nitrogen atmospheric pressure glow discharge, J. Appl. Polym. Sci. 94 (3), 1291, 2004.

[8] *L. Paralı.* The electret effects of crystallized polymer–ferropiezoelectric composite under electric discharge plasma, J. Electrostatics. 76, 89, 2015.

[9] *Novák, G.K. Elyashevichb, I. Chodák, A.S. Olifirenko, M.Števiar, M.Špírková, N. Saprykina, E. Vlasova, A. Kleinová.* Polymer matrix of polyethylene porous films functionalized by electrical discharge plasma, European Polym. Journal 44, 2702, 2008.

[10] *F.Arefi-Khonsaria, M. Tatouliana, F. Bretagnola, O. Bouloussab, F. Rondelez.* Processing of polymers by plasma technologies, J. Surface & Coatings Technol. 200, 14, 2005. DOI:10.1016/j.surfcoat.2005.02.184

[11] *M. Tahara, N.K. Cuong, Y. Nakashima.* Improvement in adhesion of polyethylene by glow-discharge plasma. Surface and Coatings Technol. 174–175, 826, 2003.

[12] *R. Morent, N. De Geyter, T. Jacobs, S. Van Vlierberghe, P. Dubruel, C. Leys, E. Schacht.* Plasma-polymerization of HMDSO using an atmospheric Pressure dielectric barrier discharge plasma process Polym. 6 (1), 537, 2009.

[13] *M.A. Kurbanov, V.A. Gol'dade, S.V. Zotov, I. S. Ramazanova, A.F. Nuraliev, F.F. Yakhyaev, U.V. Yusifova, B.G. Khudayarov*. Generation of craze-formation centers in polymer films under the action of electric discharge plasma. Technical Physics 63(7), 965 (2018).

[14] *M.A. Kurbanov, I.S. Sultanakhmedova, É.A. Kerimov, Kh.S. Aliev, G.G. Aliev, G.M. Geidarov.* Plasma crystallization of polymer–ferroelectric/piezoelectric ceramic composites and their piezoelectric properties. Physics of the Solid State 51(6), 1223, 2009.

Received: 17.07.2024

INVESTIGATION OF THE EFFECT OF SULPHUR ON THE PROPERTIES OF CARBON NANOTUBES

HASANOV ROVSHAN FARHAD
Institute of Physics of the Ministry of Science and Education of the Republic of Azerbaijan
rovshen_1989@mail.ru

However, sulphur has been made use of as a promoter for carbon nanotubes (CNTs) synthesis for many years, a clear understanding of the sulphur effect (essentially, for efficient nanotube production) is still challenging. In this report, we intend to discuss the essential role of sulphur in an Aerosol–assisted chemical vapor deposition (CVD) CNTs synthesis. Though sulphur is not incorporated into the CNTs structure, its presence, however, indirectly affects the yield, nanotube thickness, and even defines a transition between single–, double–, and multi–walled CNTs. Scanning Electron Microscope (SEM), Transmission Electron Microscopy (TEM), and Raman Spectroscopy analyses were carried out in order to investigate the complex role of sulphur in CNTs synthesis. The effect of sulphur addition as a promoter on the growth of CNTs and attempted to provide insights into the role of sulphur during CNTs formation via catalyst characterization has been investigated.

Keywords: Carbon nanotubes (CNTs), Sulphur, SEM, TEM, Raman Spectroscopy.
PACS: 61.46. Fg, 88.30. rh, 81.16. Hc, 81.15. Gh, 68.37. Hk, 68.37. Lp, 74.25. nd.

INTRODUCTION

Sulphur and sulphur–containing compounds are widely considered as a material for numerous technologies vital for our civilization: steam methane reforming, water gas shift reaction, and cracking/reforming of hydrocarbons. Ever since then, discovering of carbon nanotubes (CNTs) by the Japanese scientist Sumio Iijima in 1991 [1], these carbon nanostructures and carbon nanomaterials have been the area of great interest and potensial applications in many different fields. High quality carbon nanotubes (CNTs) possess tremendous potential for a variety of a leading applications such as catalyst supports [2], composites [3], drug delivery [4], membranes [5], sensors [6], electrodes [7], capacitors [8], etc. As it is known, CNTs are graphite layers of cylindrical shape, composed of graphitic carbon and rolled into the tubes. In addition, the type of CNTs depends on the orientation of the graphene sheet in the form of a cylinder. This can be expressed in terms of a quantity that defines how the graphene sheet is folded – a quantity called the chirality vector (C_h). The concept of chirality is one of the main factors in determining the electrical properties of CNTs. CNTs have a number of electrical, thermal, and structural properties, and these properties can be changed depending on the physical design of the CNTs. The chirality vector is defined by two integers (n, m) and is expressed as the following formula:

$$C_h = na_1 + ma_2$$

Generally, according to the number of external (outer) walls and atomic structure, CNTs are divided into three types: single–walled (SWCNTs), double–walled (DWCNTs), and multi–walled (MWCNTs).

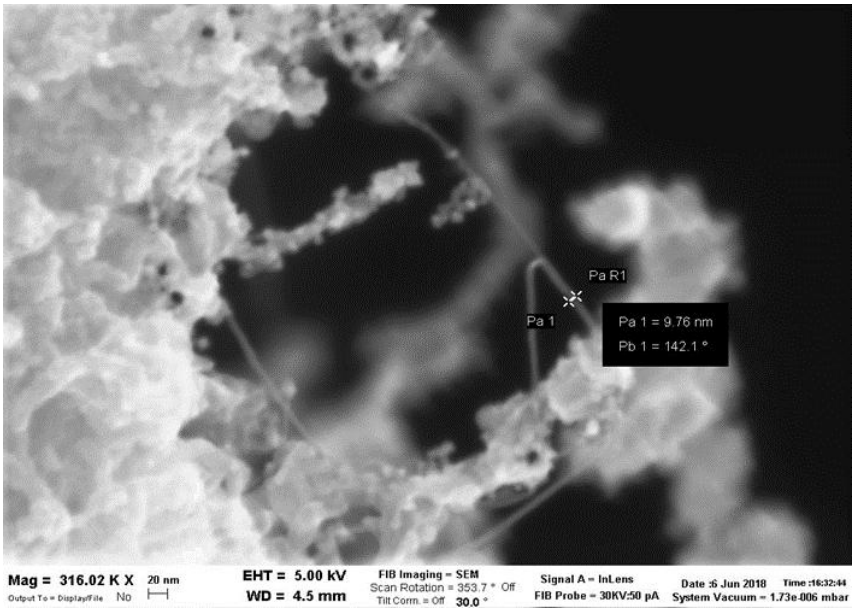

Fig. 1. SEM analysis method of synthesized CNTs using sulphur.

131, H.Javid ave, AZ-1143, Baku
Institute of Physics
E-mail: jophphysics@gmail.com

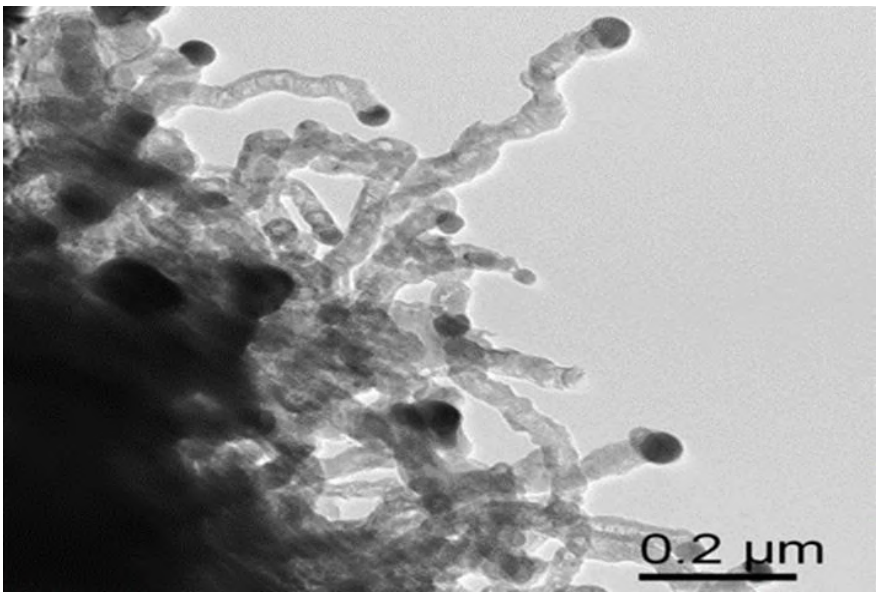

Fig. 2. TEM analysis method of synthesized CNTs using sulphur.

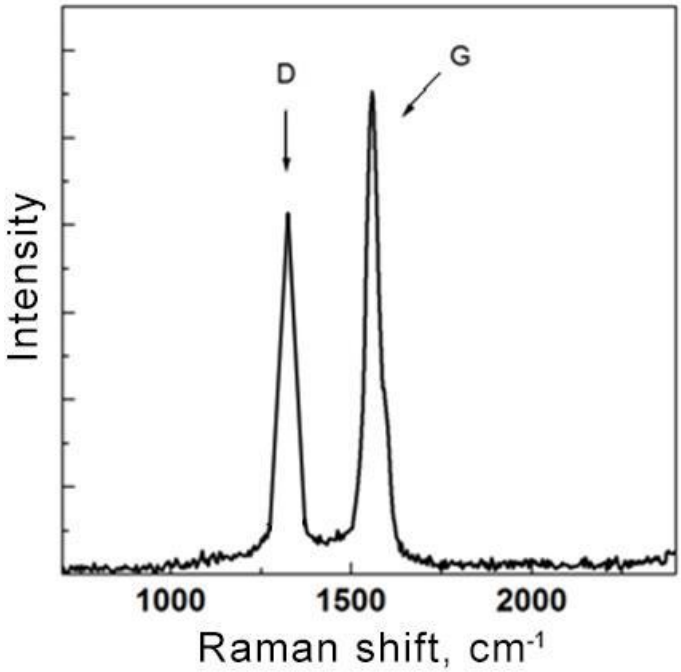

Fig. 3. Raman spectroscopic analyses of synthesized CNTs using sulphur.

However, the leading and most important structures in carbon nanotubes are SWCNTs and MWCNTs. It should be noted that, CNTs have sp^2 – hybridization state as in graphite, and each atom in this compound is combined with three other neighboring atoms. Besides having metallic and semiconducting properties, CNTs also have a strong influence on the electrical, mechanical strength, absorption and many other properties of polymers.

Accordingly, several processes to synthesize CNTs like electric arc–discharge, laser ablation, flame process, chemical vapor deposition (CVD) and others, have been proposed to date. Among these methods, CVD process can be regarded as a most potential candidate. CNTs prepared by this method are added to electric, dielectric, catalyst, polymer materials with the aim of increasing their strength and conductivity, and the obtained nanocomposite material has a number of important properties and advantages. In addition to metal catalysts, the small amount of sulphur (or sulphur–containing compounds) is used as growth promoters.

Elements of the 16th group (chalcogens) like, sulphur (S), selenium (Se), and tellurium (Te), etc., also have been widely proposed as effective promoters. Sulphur is a well–known additive to metals in various fields of science and technology: from metallurgy and steelmaking to the synthesis of carbon nanostructures. S and Se might cause an increase in the diameter and even may lead to a shift in the chiral distribution of CNTs.

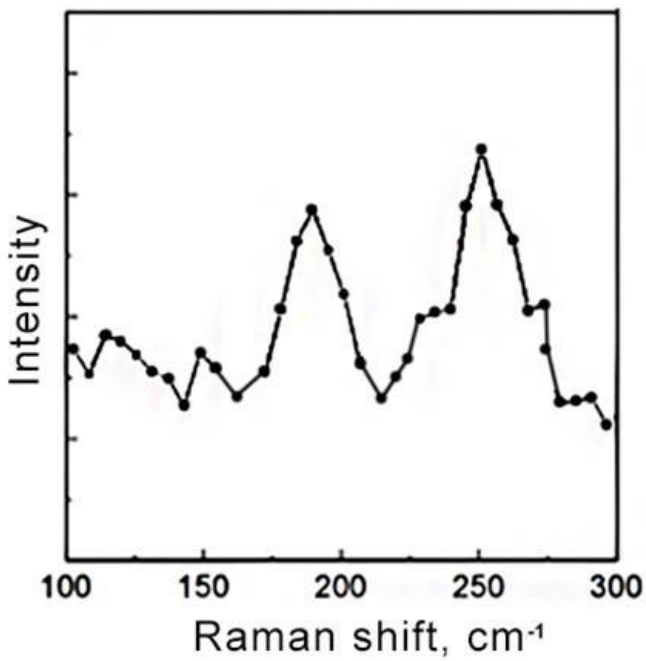

Fig. 4. RBM peaks of synthesized CNTs using sulphur.

However, sulphur is the most widely used promoter for the CNT growth and, therefore, might open a new insight into the mechanisms of the CNT formation. Also, it was determined that the addition of sulphur to the reaction solution dramatically affects the number of walls, morphology and even electrical properties of the synthesized CNTs. In addition, it was determined that a large amount of sulphur in the reagent mixture leads to the formation of amorphous carbon, and a small amount of sulphur leads to the formation of CNTs and other carbon compounds. In previous works [9], many scientists have synthesized CNTs by CVD method using ferrocene ($Fe(C_5H_5)_2$) and sulphur (S_2) as catalyst precursor and growth promoter, respectively, and m–xylene as hydrocarbon source in their investigations. However, in our carried–out works, it was shown that CNTs were synthesized by Aerosol–assisted chemical vapor deposition (AACVD) using ferrocene ($Fe(C_5H_5)_2$) and sulphur as a catalyst precursor and growth promoter, respectively, and xylene (C_8H_{10}) was used as the hydrocarbon feedstock. Using a ferrocene/sulphur/xylene solution with a relative concentration of n = 20 mg/ml, different types of carbon nanotube materials were prepared in the temperature range of $T = 850 - 1000$ ℃ in the AACVD experimental setup.

All these experiments were carried out in order to analyze the influence of sulphur on the growth process of CNTs and their parameters. The results of the experiments show that when sulphur is not included, the final sample is obtained in the form of powder, and after the introduction of sulphur, it is obtained in the form of twisted graphite thin films. For this reason, SEM, TEM, and Raman spectroscopy analysis methods were performed to determine the structure of the synthesized CNTs. When these films are researched by means of the SEM analysis method (Fig. 1), small – sized ($d = 4 - 5\ nm$) CNTs are observed. However, apart from that, TEM analysis method (Fig. 2) were performed to determine the structure of the obtained CNTs. During the TEM analysis, small diameter CNTs were seen among the CNTs with a diameter ranging from 10 to 30 nm. Considering into account all these facts, Raman spectroscopic analyses (Fig. 3) of the obtained samples were performed. As can be seen from this spectrum, in addition to the D (1340 cm^{-1}) and G (1570 cm^{-1}) peaks belonging to graphite, the Radial Breathing Mode (RBM) peak (Fig. 4), X_{RBM} = 180 ÷ 250 cm^{-1}, characteristic of SWCNTs was observed in the wavenumber interval. The frequency of the RBM mode directly depends on the diameter of the CNTs in the form of the following relationship:

$$\omega_{RBM} = \frac{A}{d} + B$$

This also proves the existence of nanotubes with a diameter of d = 1 ÷ 1.3 nm. As for the crystallinity properties of the grown product, here we have used the ratio of the intensities of the D (defect) and G (graphite) peaks. So, as a result of calculations, the ratio of I_D to I_G was equal to 0.42 (I_D/I_G = 0.42).

[1] *S. Iijima.* Helical microtubules of graphitic carbon, J. Nature 354 (1991) 56–58.

[2] [2] *N. Coustel, B. Coq, P.M. Ajayan,* et al. Application of carbon nanotubes as supports in heterogeneous catalysis, J. Am. Chem. Soc. 116 (1994) 7935–7936.

[3] *R. Andrews, M.C. Weisenberger.* Carbon nanotube polymer composites, J. Curr. Opin. Solid State Mater. Science 8 (2004) 31–37.
[4] *A. Bianco, K. Kostarelos, M. Prato.* Applications of carbon nanotubes in drug delivery, J. Curr. Opin. Chem. Biol. 9 (2005) 674–679.
[5] *Ihsan Ullah.* Carbon nanotube membranes for water purification: developments, challenges, and prospects for the future, J. Sep. Purif. Technol. 209 (2019) 307–337.
[6] *I.V. Zaporotskova, N.P. Boroznina, Y.N. Parkhomenko, L.V. Kozhitov.* Carbon nanotubes: sensor properties. A review, Mod. Electron. Mater. 2 (2016) 95–105.
[7] *Y. Zhou, Y. Zhu, B. Xu, X. Zhang.* High electroactive material loading on a carbon nanotube/carbon nanofiber as an advanced free–standing electrode for asymmetric supercapacitors, J. Chem. Commun. 55 (2019) 4083–4086.
[8] *L.F. Aval, M. Ghoranneviss,* et al. High–performance supercapacitors based on the carbon nanotubes, graphene and graphite nanoparticles electrodes, J. Heliyon 4, (2018) e00862.
[9] *A. Barreiro, C. Kramberger,* et al. Control of the single–wall carbon nanotube mean diameter in sulphur promoted aerosol–assisted chemical vapor deposition, J. Carbon 45 (2007) 55–61.

Received: 05.09.2024

THE CONNECTION BETWEEN THE ENERGY AND STRUCTURAL COMPLEXITY OF THE MATTER, STRUCTURAL COMPLEXITY ORIGIN OF THE ELECTROWEAK BOSON MASSES AS WELL AS METABOLISM IN LIVING ORGANISMS

FIZULI MAMEDOV
Institute for Physical Problems, Baku State University, Azerbaijan
e-mail: mail.quanta02@gmail.com, phone: (994) 12 510 18 22

The connection between the energy and structural complexity of the materials is discussed in terms of the crystals of the different chemical elements, the latent heat of fusion and crystal structure connection is analyzed. This type of connection equation paves a way to calculating the electroweak gauge boson masses in an alternative way, on the basis of the same concepts. Specific values of the parameters for carbon crystals, water, lithium and beryllium are analyzed which sheds light to the origin of the cancer disease. The right - handed neutrino question and the strong CP problem in quantum chromodynamics are also analyzed in the context of the symmetry changes, phase transitions at the early stages of the formation of the universe.

Keywords: dependence of the structural complexity on the energy, structural complexity - latent heat of fusion connection of the substances, the connection between the charges and masses of the elementary particles.
PACS: 14.70.Hp, 12.15.−y, 12.15.Lk, 12.20.−m, 12.38.−t, 12.60.−I

INTRODUCTION

A quick look at the parameters of the elementary particles tells us that the connection between the mass and coupling constant discussed in the previous works for the electroweak gauge bosons

$$M_W/g = M_B/g' \qquad (1)$$

is present for all the known elementary particles, but only in an approximate form. For the second and third generation of quarks up quarks are significantly heavier than down quarks. Electroneutral neutrinos have no mass or tiny mass only. The exact nature of Eq.(1) indicates that the electroweak gauge bosons are indeed the fundamental level of particles, the intermediaries of the fundamental level of interactions. This equation can be interpreted as follows: the bigger the energy (mass) of the system, the bigger the value of the coupling constant and hence the higher the structural complexity of the system where these interactions occur.

Charge conjugation operator aspect of the electron wave function also confirms this interpretation of the equation above. Charge conjugation operator changes a negative - energy solution for the electron with the certain momentum p_i and polarization S_i to a positive - energy solution with the same p_i and S_i:

$$\Psi_C = C\gamma_0\Psi^* = C\gamma_0((\varepsilon\gamma_i p^i + m)/(2m))^*(1 + \gamma^5(p_i S^i)/2)^*\Psi^* \rightarrow (-\varepsilon\gamma_i p^i + m)/(2m)(1 + \gamma^5(p_i S^i)2)\Psi_C \qquad (2)$$

Here ε = 1 for positive energy states and ε = -1 for negative energy states.

When applied to Eq.(1), we can say that both numerator and denominator change sign which has no impact on the equation.

METHODS

A. The connection between the structural complexity and latent heat of fusion for crystals

We can observe a similar mass - coupling constant connection tendency relating to the values of the atomic nuclei masses. Iron and Nickel have the biggest binding energy per nucleon which means relatively small nuclear mass. Nickel has face centered cubic crystal structure, Iron has body centered cubic crystals and face centered cubic crystals: the nucleus with the smaller mass can accommodate relatively simpler crystal form only. One can explain this with the smaller interaction force between the nuclei. Certainly one can explain this a slightly different way. Iron nuclei have relatively small nuclear size, approximately 3.7 fm: they experienced the shift in the symmetry process in a lesser degree [3] and they tend to have simpler crystal structure. Gold nuclei with slightly smaller binding energy per nucleon can accommodate more complex forms of crystal structure. The connection between the structural complexity and energy of the system reveals itself in a different form when we look at the values of the latent heat of fusion of the chemical elements. Both diamond and graphite crystals of carbon (the most abundant forms of carbon) have noticeably high latent heat of fusion, around 120 kJ/mol. Both of these one chemical element based crystals have the higher melting temperature than any other one chemical element based crystal. Carbon is at the core of the organic substances, the substances that give rise to the life on Earth, to the most complex structures in the universe. The major ingredients of life, carbohydrates, fats and proteins contain a large portion of the hydrogen atoms besides the carbon atoms. What is more important here, the simple structure of the hydrogen atoms or the fact that hydrogen H_2 has the lowest melting point among the chemically active one

131, H.Javid ave, AZ-1143, Baku
Institute of Physics
E-mail: jophphysics@gmail.com

chemical element based substances? Combination of the element with the highest melting point (3652 ºC) for the graphite) and with the lowest melting point might give rise to an enormous flexibility in chemical reactions keeping the structural complexity of the molecule essentially intact. 20 ºC is considered optimal condition for life on Earth. Small departures from this temperature would not also affect significantly the complexity type of the molecule.

Perhaps it is not accidental that Lithium which is used for the treatment of the nervous disorders has a latent heat per gram close to that of water, 422 J/g vs 334 J/g. Lithium has smaller value for the latent per mole than that of water. This can be considered as an indication of even closer values for the latent heat of these two substances. Lithium also prevents the development of different cancers. The next to lithium chemical element, Berillium has relatively high latent heat per gram, 1350 J/g and is considered as carcinogenic. One would say that Berillium's crystal making tendency is significantly different from the structural complexity that the living creatures strive to have (see also [3] for the interpretation of the peculiar values of the binding energies per nucleon for the Lithium and Beryllium). Liquid (one - dimensional) crystal properties of the human DNA have been known for a very long time.

It is natural to expect that the human DNA's and water's structural complexity making tendencies are close to each other. Magnesium is a chemical element with both the molecular mass and latent heat of fusion slightly bigger than those of water, 24.3 a.u. vs 18 a.u and 8.48 kJ/mol vs 6.02 kJ/mol. Magnesium has a numerous health benefits and low level of magnesium in human body leads to the cancer disease. From the other side, Lithium, Beryllium and Magnesium's role in the human health conditions also tells us about the strong connection between the chemical substance's structural complexity making tendencies and their latent heat of fusion.

B. The connection between the structural complexity and elementary particle's mass in quantum field theory

Do we have a certain etalon or maximum of the structural complexity of the systems for our particular universe that all the living creatures strive to achieve (by their own approach to this goal)? If yes, this complexity type must be at the core of the electroweak gauge boson masses too. As the universe expands and cools at the early stages of its formation it gains an opportunity to accommodate more complex structures/particles at some point. The original $SU(2)_L$ x $SU(2)_R$ symmetry is replaced by the U(1) gauge symmetry that we observe around today [1]. The original $SU(2)_L$ x $SU(2)_R$ symmetry based calculations and the Standard Model make the same predictions for the W and Z boson masses. Notice that these predictions are independent of the interactions with the Higgs particle and its mass. A plenty of information available on the latent heat of fusion and crystal structures of the one chemical element based substances could be used for further clarification of this pivotal connection between the structural complexity of the systems and their energy, in other words, for bringing some clarity to the question what approximations and priorities does the nature use for choosing this or another crystal structure.

A few words about the role of the group theory in the structural complexity analysis. Perhaps the existing group theory needs to be expanded and made more versatile to achieve this goal. The fruitful character aspect of the group theory is a quite promising venue in this sense. One can consider the character for the given irreducible representation as bringing the state vectors of a system to one dimensional space. Liquids can be considered as one dimensional crystals to some extent. If you isolate two molecules of the liquid and consider their motion along the circle with the center in the midst of them it would not change the interaction force between them and this is an allowed motion for the liquid molecules. One needs such a decomposition of the original irreducible representations that the small variations of the parameters of the subgroups would have an impact on their complexity aspect.

Due to $SU(2)_L$ x $SU(2)_R$ symmetry originally both left - handed and right - handed fermions interact with the triplet of electroweak vector bosons W. After the first stage of the shift in the symmetry, after meltdown (rapid decay) of the right – handed fermion doublets the fermion – electroweak gauge boson interaction part of the Lagrangian obtains the form which the Standard Model based theories consider as a starting point of symmetry breaking:

$$\mathrm{L}_{int} = \mathrm{i}\bar{\mathrm{R}}\gamma^i(\partial_i + \mathrm{ig}'\mathrm{B}_i - (\mathrm{i}/2)\mathrm{g}\sigma^l\mathrm{W}_i^l)\mathrm{R} + \mathrm{i}\bar{\mathrm{L}}\gamma^i(\partial_i + \mathrm{ig}'\mathrm{B}_i - (\mathrm{i}/2)\mathrm{g}\sigma^l\mathrm{W}_i^l)\mathrm{L} \rightarrow$$

$$\mathrm{i}\bar{\mathrm{R}}\gamma^i(\partial_i + \mathrm{ig}'\mathrm{B}_i)\mathrm{R} + \mathrm{i}\bar{\mathrm{L}}\gamma^i(\partial_i + \mathrm{ig}'\mathrm{B}_i - (\mathrm{i}/2)\mathrm{g}\sigma^l\mathrm{W}_i^l)\mathrm{L} \qquad (3)$$

Meltdown of the right - handed doublet looks similar to getting character of the given representation discussed above. Isospin aspect and B_i field aspect of the state vector merge together, isospin doublet disappears This merge does not affect the electric charge of the right - handed fermions which is the sum of the isospin quantum number I_W and hypercharge Y. But the structural complexity of the system certainly gets altered. Right –handed neutrinos disappear. Right - handed fermions no longer interact with the W bosons. $SU(2)_L$ x $SU(2)_R$ fermion symmetry model readily explains the absence of right - handed neutrinos in the experiments and somewhat odd hypercharge numbers of the right - handed quarks. It is not because of different values of hypercharge that right -handed quarks do not form a doublet. Contrary, because of the meltdown of the isodoublet right - handed quarks get these hypercharge numbers. The Standard Model procedure of getting the Z_μ boson and photon A_μ structures from the covariant derivative of the Higgs

field is also simply bringing into one dimension the isospin doublet related structure of the W bosons. According to the fermionic origin of the gauge bosons theory gauge transformations are not simply mathematical transformations: they reflect the change of the phase factor of the fermionic wave functions [3]. The probability is essentially zero that nature will choose some particular gauge of the local SU(2) symmetry out of infinite number options, the gauge which would produce the desired W boson and B_μ boson mixing. It is the meltdown of the right - handed fermion doublets that leads to the W boson and Z_μ boson mixing.

The d quark is heavier than the u quark and we do not see Eq. (1) type mass - coupling constant relation in this particular case which could be the result of restoration of the original $SU(2)_L$ x $SU(2)_R$ symmetry for the significant interval of the strong interactions of these quarks. This aspect of the light quarks also sheds light to the strong CP problem in quantum chromodynamics.

We can describe the emergence of the Z_μ boson and photon A_μ after redistribution of the masses of the original

electroweak bosons by using the Dirac bra - ket formalism (see also [1]). The W bosons and the B boson belong to the triplet and the singlet states of the two spin ½ particles and this reveals itself manifestly in the Dirac bra - ket formalism. Here we treat Dirac ket vectors |> as the vectors pointing in the certain direction in the quantum mechanical state space to get a clear idea about the Z_μ boson, photon A_μ structures and Z boson - W boson mass connection (Z_μ boson mass - electroweak interactions coupling constants connection).

$$\mathrm{M_W^2}\,|\mathrm{W_1}\rangle|\mathrm{W_1}\rangle + \mathrm{M_W^2}\,|\mathrm{W_2}\rangle|\mathrm{W_2}\rangle + \mathrm{M_W^2}\,|\mathrm{W_3}\rangle|\mathrm{W_3}\rangle + \mathrm{M_B^2}\,|\mathrm{B}\rangle|\mathrm{B}\rangle =$$

$$\mathrm{M_W^2}\,|\mathrm{W_1}\rangle|\mathrm{W_1}\rangle + \mathrm{M_W^2}\,|\mathrm{W_2}\rangle|\mathrm{W_2}\rangle + \mathrm{M_W^2}/\mathrm{g}^2(\mathrm{g}^2|\mathrm{W_3}\rangle|\mathrm{W_3}\rangle + \mathrm{g}'^2\,|\mathrm{B}\rangle|\mathrm{B}\rangle) =$$

$$\mathrm{M_W^2}\,|\mathrm{W_1}\rangle|\mathrm{W_1}\rangle + \mathrm{M_W^2}\,|\mathrm{W_2}\rangle|\mathrm{W_2}\rangle + \mathrm{M_W^2}/\mathrm{g}^2(\mathrm{g}|\mathrm{W_3}\rangle - \mathrm{g}'\,|\mathrm{B}\rangle)^2 +$$

$$4\,(\mathrm{M_W^2}/\mathrm{g}^2)\mathrm{gg}'|\mathrm{W_3}\rangle|\mathrm{B}\rangle = \mathrm{M_W^2}\,|\mathrm{W}^+\rangle|\mathrm{W}^-\rangle + \mathrm{M_Z^2}\,|\mathrm{Z}\rangle|\mathrm{Z}\rangle \qquad (4)$$

with $\mathrm{M_Z} = \mathrm{M_W}/\sqrt{\frac{\mathrm{g}^2}{\mathrm{g}^2+\mathrm{g}'^2}} = \mathrm{M_W}/\cos\theta_\mathrm{W}$ and

$|\mathrm{Z}\rangle = (\mathrm{g}|\mathrm{W_3}\rangle - \mathrm{g}'\,|\mathrm{B}\rangle)/\sqrt{\mathrm{g}^2 + \mathrm{g}'^2} = |\mathrm{W_3}\rangle\cos\theta_\mathrm{W} - |\mathrm{B}\rangle\sin\theta_\mathrm{W}$

$\cos\theta_\mathrm{W} = \frac{g}{\sqrt{\mathrm{g}^2+\mathrm{g}'^2}}$ is the Weinberg angle here.

The $(\mathrm{M_W^2}/\mathrm{g}^2)\mathrm{gg}'|\mathrm{W_3}\rangle|\mathrm{B}\rangle$ term in the equation above disappears because of orthogonality of $|\mathrm{W_3}\rangle$ and $|\mathrm{B}\rangle$ states.

In reality everything could be more complex during the phase transitions at the early stages of the formation of the universe than this presented picture of the phase transitions. This is a multistage phase transition process similar to the cell division process. Many facts tells us that shift in the symmetry process is a second order phase transformations type. Coupling constants would disappear from the interaction Lagrangian if we use its Eq. (3) form and represent electroweak gauge bosons as fused states of fermions [3]. One can interpret this as a sign of the presence of the long range correlations. Right - handed quarks and electron preserve an important aspect of their structural complexity, their electric charge during the phase transition process which is an indication of the no latent heat of 'fusion' process, the second order phase transition process.

DISCUSSION AND CONCLUSIONS

The equation connecting electroweak interactions coupling constants and electroweak boson masses is just one manifestation of the much broader connection between the energy and structural complexity of the quantum mechanical systems. Structures of the different crystals and their latent heat of the fusion values are analyzed for this purpose. It is emphasized that phase transitions, symmetry changes during early stages of the universe's formation are complex, multistage process. It is also pointed out that the original $SU(2)_L$ x $SU(2)_R$ fermion symmetry approach to these phase transitions answers the question of the absence of the right – handed neutrinos and sheds light to the strong CP problem in quantum chromodynamics. Somewhat odd values of the right - handed quarks are naturally explained by the meltdown of the right - handed isodoublets in this work.

ACKNOWLEDGEMENTS

The author would like to thank Sadiyar Rahimov, director of the Institute for the Physical Problems, Baku State University, for the several helpful discussions of the phase transitions in crystals.

[1] *F. Mamedov*. Particle interactions, masses and the symmetry breaking, hep-ph/0606255

[2] *F. Mamedov*. Fermion masses and the symmetry breaking; Strong interactions spin quantum number as the unifier of the strong and electroweak interactions, hep-ph/0607010

[3] *F.A. Mamedov*. $SU(2)_L$ x $SU(2)_R$ symmetry of the fermions and the vector bosons, the

fermionic origin of the local gauge transformations, the visible traces of the flickering nature of the early stages of the universe's formation, AJP Fizika C, 2023

[4] *F.A. Mamedov*. Scaling properties of Dirac matrices, the gravitational field, and consistently life like transformation law behavior aspect of these matrices. Dirac matrices and dark matter, AJP Fizika E, 2024.

[5] *S. L. Glashow*. Partial Symmetries of Weak Interactions, Nuclear Physics 22, (1961), 579.

[6] *S. Weinberg*. A Model of Leptons, Physical Review Letters, 19, 1264

[7] *A. Salam*. \textit{Svartholm, N, Proceedings of the Eighth Nobel Symposium, Almqvist & Wiksell, Stockholm} (1968)

[8] *S. Eidelman* et al., Phys. Lett. B 592, 1 (2004).

[9] *Sam Walters*. How Eintstein Got His Field Equations, arxiv.org/abs/1608.05752

[10] *P. Salucci, A.Burkert*. Dark Matter Scaling Relations, arXiv:astro-ph/0004397

[11] Collaboration, CMS (2019). "Evidence for light-by-light scattering and searches for axion-like particles in ultraperipheral PbPb collisions at $/s_{NN}$ = 5.02 TeV", Phys. Lett. B. 797: 134826. arXiv:1810.04602. doi:10.1016/j.physletb.2019.134826. S2CID 201698459

[12] *R.W. Brown, K.L. Kowalski, and S.J. Brodsky*. Classical radiation zeros in gauge theory amplitudes, Phys. Rev. D, 28:624, 1983.

[13] Size of helium nucleus measured more precisely than ever before. https://www.admin.ch/gov/en/start/documentation/media-releases.msg-id-82143.html

[14] Size of a Nucleus, Nucleus of Lithium-7. http://fafnir.phyast.pitt.edu/particles/sizes-3.html

[15] National Superconducting Cyclotron Laboratory, Laser precision studies of the nuclear radii. http://nscl.msu.edu/news/news -25.html

Received: 25.09.2024

THE INVESTIGATION OF THE VOLTAGE AND FREQUENCY DEPENDENT ELECTRICAL CHARACTERISTICS OF Re/n-GaAs SCHOTTKY BARRIER DIODE USING I–V, C–V AND G/ω–V MEASUREMENTS

I.M. AFANDIYEVA[1*], S.A. YERISHKIN[2], E.A. RASULOV[1], S.I. AMIROVA[1]

[1]Baku State University, AZ1148, Baku, Azerbaijan

[2]Department of Chemical Engineering, Faculty of Engineering, Gazi University, Ankara, Turkey

**Corresponding author: E-mail address: I_afandiyeva@yahoo.com*

Tel: +994 12 539 85 82 / +994 50 396 76 41

The main parameters of Re/n-GaAs Schottky barrier diodes (SBDs) were investigated at room temperature by the forward and reverse bias current–voltage (I–V), capacitance–voltage (C–V) and conductance–voltage (C/ω − V).The diodes were fabricated by using PLD technique. Characteristics parameters such as potential barrier height (Φ_B), ideality factor (n) and series resistance (R_s) have been calculated by using different methods and compared. Furthermore, the voltage-dependent profile of the resistance (R_i) and shunt resistance (R_{sh}) were obtained for Re/n-GaAs Schottky diodes from the $I-V$ data using Ohm's law. In addition, the influence of frequency on parameters have been investigated. From the reverse bias C^{-2} versus V plots the Fermi energy level E_F, doping concentration N_D and potential barrier height for each frequency have been obtained. The dependence of parameters on frequency due to surface state have been revealed.

Keywords: Re/n-GaAs Schottky barrier diodes (SBDs); Frequency dependence; Series resistance; Surface states, Impedance spectroscopy;
PACS:73.30+y, 73.20.At, 73.40.Ns

1. INTRODUCTION

Currently, an important element of most electronic devices are contact structures based on Schottky barriers. In this regard it should be noted that the electrical properties and fabrication of SBDs very interesting both in electronic applications and in understanding other semiconductor devices. It should be noted, that basic parameters of electronic devices depend on technology of fabrication, choice of materials, doping degree and surface states of semiconductor [1-4]. Besides the using of different theoretic and calculation methods also influence on obtained result.

Shottky barrier diodes on the basis of GaAs are an important element in many electronic devices. This is determined largely by the relative ease of the fabrication of metal-semiconductor contacts and some advantages in comparison with p-n junction such as high electron mobility, high voltage electrical breakdown, high radiation resistance. GaAs has a high electrical resistivity as well as a high dielectric constant. Unlike silicon devices, devices on the basis of GaAs are less susceptible to temperature changes and generate less noise when operating at high frequencies. Due to these properties, direct-gap semiconductor GaAs is widely used in semiconductor lasers, some radar systems, in solar batteries, working in space [5-8].

Due to high melting point, chemical resistance, catalytic activity, stability at high temperatures, high stability of films, a low temperature coefficient of resistance, a slight change in resistance with increasing film thickness rhenium is an interesting material [9-13]. However, in the scientific literature there is practically no information on studying the parameters of SBD Re/n-GaAs [14,15]. The aim of this study is investigation of main parameters of Re/n-GaAs on the basis of measured $I-V$, C-V and G/ω-V characteristic at room temperature.

EXPERIMENTAL PROCEDURE

Investigated Re/n-GaAs SBD-s were fabricated using the DSP (double si depolished) method. Single-crystal n-type GaAs (100) with a thickness of 625 μm and carrier concentration (2.2-3.1)10^{18} cm^{-3} was used as a semiconductor substrate. After numerous degreasing and processing steps, the GaAs wafer was thoroughly washed in deionized water with a resistivity of 18,2 MΩ cm. Low ohmic contacts to the n-GaAs wafer were fabricated using high purity (99.999%) Au. In a high vacuum system of about 10^{-6} Torr, Au with a thickness of about 2000 Å was deposited on the entire back side of the n-GaAs wafer. The ohmic contacts were annealed by a temperature treatment at 450 ºC for 5 min [15].

Rectifying contacts with a thickness of about (200-250) nm were deposited by PLD onto the front surface of an n-type GaAs wafer. Rhenium (Re), which was used as the target material, was supplied by Good fellow with a 99.99% purity.

Before starting material deposition, vacuum was pumped down to a base pressure about 1x10^{-7}mbar using a DUO 20M Rotary Vane Pump connected to a HiPace 700 turbo molecular pump, both of them made by Pfeiffer Vacuum. When deposition was started, the chamber pressure was about 1x10^{-6} mbar. To fabrication of rectifying contacts with 1.5 mm diameters a metal shadow mask was used. Deposition time was about 2 hours depending on the required

131, H.Javid ave, AZ-1143, Baku
Institute of Physics
E-mail: jophphysics@gmail.com

contact material thickness. A sketch of the obtained Schottky diode structure is given in Fig. 1.

The current-voltage ($I-V$) measurements in the range from -5.0 V to +5.0 V with 5 mV steps were performed by using a Keithley 2410 Source Meter at room temperature.

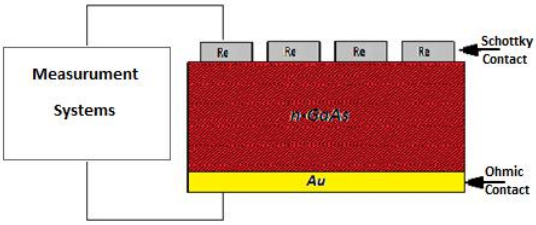

Fig.1. Cross-sectional view of Re/n-GaAs (MS) Schottky diodes/structures.

2. RESULTS AND DISCUSSION

The operation of Schottky diodes is determined mainly by the height of the potential barrier (Φ_B), the ideality factor (n) and series resistance (R_s) . It should be noted that the deviation of the structure from ideality does not allow one to unambiguously determine F and n [16-23]. To accurately determine the barrier height (BH), three factors need to be taken into account: the accuracy of measuring the initial values, the accuracy of the approximation method and the accuracy of determining the current transfer mechanism. In the present work Re/n-GaAs SBD parameters have been calculated by the using of various methods that do not require measurements at different temperatures from measurements of the current-voltage characteristics and compared.

The current-voltage characteristic of Re/n-GaAs SBD measured in the forward and reverse bias regions (±5 V) was previously analyzed based on thermionic emission theory [24]. In the presented article $I-V$ charactersistic has been analized by the depending LnI vs LnV as is shown in Fig.2. [1,16,24,25].

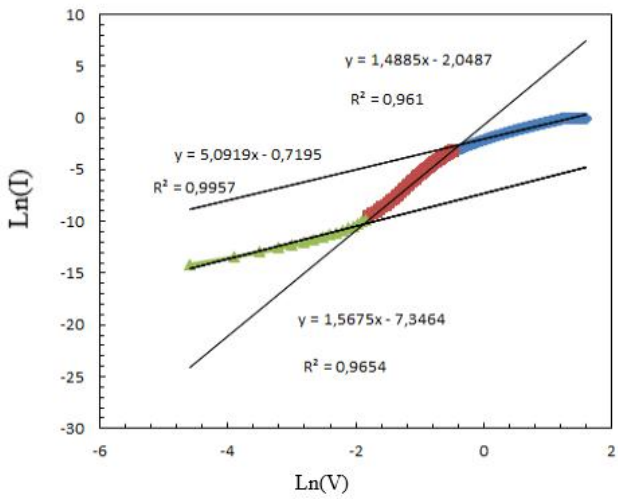

Fig.2. Double logarithmic $I-V$ plot of Re/n-GaAs SBD at forward bias.

The above method is very convenient for calculating the parameters of a diode with a narrow-gap semiconductor (GaAs). As can be seen from the Fig.2. the slope of the characteristic changes. The slope 1.48 of first region of voltage from 0.66 V to 5 V correspond to influence of series resistance. When the voltage varying from 0.17 to 0.65 V above-barrier current transfer is observed and slope is 5.09. In the third section at voltage (0.01÷0.16)V the slope equals 1.56 and can be analyzed by the presence of diffusion current transfer. Changing the slope of the characteristic does not allow to accurately determine the height of the potential barrier, ideality factor and series resistance.

To determine Φ_B and R_s the method (Norde's method) has been used [20]. It is known, that when influence of R_s is great at all values of the applied voltage Norde's functions can presented as:

$$F(V) = \frac{V}{\gamma} - \frac{kT}{q}\left[ln\left(\frac{1}{T^2}\right) - ln(A^*A)\right] \quad (1)$$

$$\Phi_{BN} = F(V_{min}) + \frac{V_{min}}{\gamma} - \frac{kT}{q} \quad (2)$$

$$R_s = \frac{(\gamma - n)kT}{qI_{min}} \quad (3)$$

where γ is a dimensionless integer greater than n [20]. In this case, to identification of potential barrier height and series resistance at room temperature for the Re/n-GaAs diode was used the minimum point of $F(V)$ vs V plot (Fig.3). The V_{min}, $F(V_{min})$, Φ_{Bn} and R_s values were found to be 0.3 V, 5.88x10^{-1} V, 0.78 eV and 4.13 Ω, respectively.

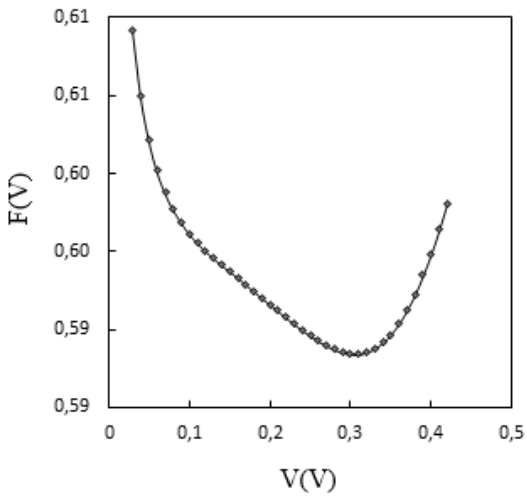

Fig.3. F(V) vs. V(V) plot of Re/n-GaAs SBD.

On the other hand, this method, along with its advantages, has some disadvantages. The difference between the ideality factor and unity affects the calculation results. Besides, according to this technique, the calculation is performed at one point of the $I-V$ characteristic, which can negatively affect the calculation accuracy.

Another way to solve the identified problem is to use the method developed by Cheung [21]. The method has been used in order to compute Re/n-GaAs SBD parameters like the Φ_B, n and R_s [16,21]. Cheung's functions can be obtained as follows

$$\frac{dV}{d(\ln I)} = n\left(\frac{kT}{q}\right) + IR_s \quad (4)$$

$$H(I) = V - n\frac{kT}{q} ln\left(\frac{I}{AA^*T^2}\right) = n\Phi_{B0} + R_s I \quad (5)$$

$$H(I) = V - n\frac{kT}{q} ln\left(\frac{I}{AA^*T^2}\right) \quad (6)$$

Here, IR_s is the voltage drop across the series resistance of the Re/n-GaAs SBD. The plots $dV/d(lnI) - I$ and $H(I) - I$ are presented in Fig.4 Using the slope of $dV/d(lnI) - I$ has been obtained R_s and n as 3.27 Ω and 1.43, respectively by using Eq.(4). $I-V$ data was analyzed by the well-known equation at forward bias Eq. (5). On the basis of $H(I) - I$ plot's has been calculated R_s with the value of 4.04 Ω and potential barrier height Φ_{BCh}= 0.74 eV (Fig.4).

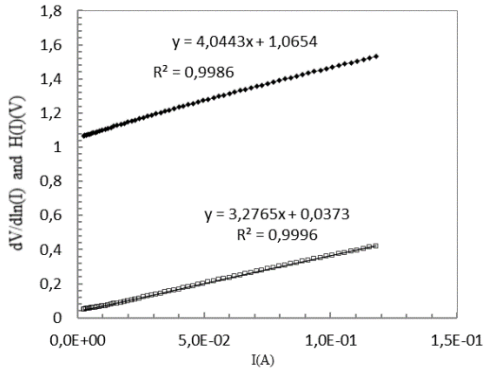

Fig.4. The plots of $dV/dlnI$ versus I and $H(I)$ versus I at room temperature.

Another method for the obtaining of series resistance and ideality factor is Verner's method [22]. In this method differential conductance ($L = dI/dV$) of real diode at $V > 3kT/q$ is described by the relation (Fig.5):

$$\frac{L}{I} = \frac{q}{nkT}(1 - R_s L) \quad (7)$$

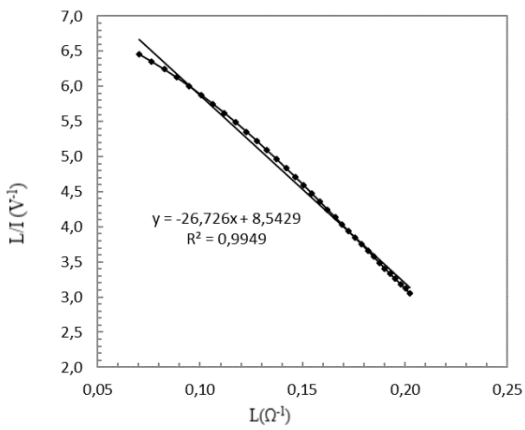

Fig.5. The plots of L/I versus L for Re/n-GaAs SBD at room temperature

Eq.7 shows that a plot of L/I versus L yields a straight line with slop R_s. From y-axis intercept one can determine the ideality factor n. We have compared the result of different methods to tested of the characteristic parameters of Re/n-GaAs SBD on the basis of experimental $I-V$ curve measured at room temperature. One can see that the different techniques give almost similar meanings of the parameters. Exception is n determined by Verner's method.

The calculated values of characteristic parameters (Φ_B, I_o, n and R_s) of Re/n-GaAs SBD experimentally obtained at room temperature are given in Table 1.

Table 1.

Φ_{B0} (eV)	n	R_s (Ω)	R_{sh}(Ω)	Norde		Cheung		Cheung		Verner	
						dV/dlnI		H(I)			
				Φ_{BN} (eV)	R_{sN} (Ω)	R_{sCh1} (Ω)	n	R_{sCh2}(Ω)	Φ_{BCh}(eV)	R_{sv}(Ω)	n
0,61	1,84	3,92	2,19E+1	0,78	4,13	3,28	1,43	4,04	0,74	3,13	4,52

The obtained result indicates the difference between the selected and ideal model. To explain the obtained results, it should be taken into account that the ratio of the lattice parameters of the metal and semiconductor plays a significant role in the formation of a contact [26]. It is known, that lattice parameters are a = 0.565nm for GaAs and a=2.761nm, c=4.456 nm for Re, respectively [27]. Due to lattice mismatch between the metal and GaAs in the subsurface region of semiconductor elastic stresses can be appear. At metal deposition on the semiconductor surface is possible a mutual diffusion of metal and semiconductor atoms, which affects the formation of a barrier and surface states [28-30]. The obtained difference between values of parameters Φ_B, n and R_s, calculated with the using of different methods can be attributed to formation of barrier and surface states due to influence of lattice mismatch between Re and GaAs. In connection with this goal, the Re/n-GaAs SBD were studied by the impedance method at frequencies of the test signal (50 mV) 10 kHz - 5 MHz. So, figure 6 shows for Re/n-GaAs SBD the dependence of C(a) and G/ω (b) value vs. frequency at fixed voltage and room temperature. It should be noted, that decreasing of values of C and G/ω at height frequencies can be attributed to the carrier charges at surface states/traps and their relaxation time (τ).

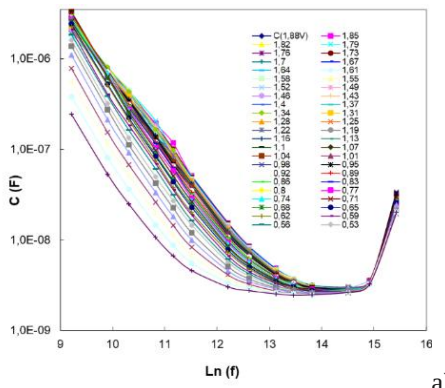

a)

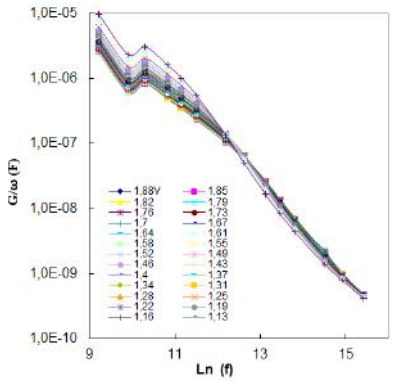

b)

Fig. 6. The dependence of C(a) and G/w(b) value vs. frequency at fixed voltage for Re/n-GaAs SBD (T=300K).

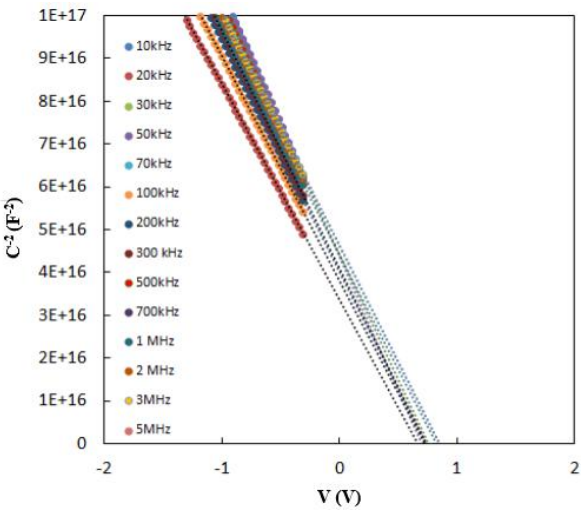

Fig.7. C^{-2}–V plot of Re/GaAs Schottky diode at various frequencies (10kHz-5MHz).

Table 2.

Various parameters for Re/GaAs Schottky diode obtained on the basis of the of C-V and G/ω –V characteristics measured at the frequencies in the range of from 10kHz to 5MHz (50mV)

f, x10^3 Hz	V_0 (V)	N_Dx 10^{17} (cm^{-3})	E_Fx10^{-2} (V)	Φ_B (eV)	V_{max}, (V)	G/ω_{max} (F)	C_m, (F)	N_{ss}, (eV^{-1} sm^{-2})	$R_{s\ max}$, (Ω)
10	0,61	1,68	2,43	0,63	0,23	1,90E-5	2,30E-6	6,48E+13	3,01
20	0,67	2,18	1,77	0,68	0,25	3,01E-6	6,35E-7	3,18E+13	6,64
30	0,63	1,82	2,23	0,65	0,26	3,60E-6	2,68E-7	2,04E+13	5,33
50	0,69	1,75	2,32	0,72	0,28	2,12E-6	1,00E-7	8,25E+13	14,02
70	0,71	1,95	2,15	0,72	0,29	1,09E-6	6,20E-8	4,41E+13	11,46
100	0,72	2,09	1,88	0,74	0,35	5,42E-7	3,00E-8	1,83E+12	15,94
200	0,73	1,98	2,01	0,75	0,41	1,45E-7	1,06E-8	7,02E+11	20,95
300	0,73	1,98	2,01	0,75	0,53	1,66E-8	6,50E-9	4,73E+11	38,57
500	0,75	1,88	2,14	0,77	0,54	2,38E-8	4,11E-9	3,39E+11	38,5
700	0,77	1,93	2,07	0,79	0,56	1,22E-8	3,42E-9	2,74E+11	38,30
1000	0,82	2,06	1,91	0,84	0,58	6,66E-9	2,91E-9	3,14E+11	32,7
2000	0,83	1,72	2,37	0,85	0,63	1,89E-9	2,74E-9	2,30E+11	17,83 (≠f(V)
3000	0,85	2,02	1,97	0,86	0,68	9,1E-10	3,42E-9	1,84E+11	5,28 (≠f(V)
5000	0,83	1,81	2,23	0,85	0,74	4,62E-10	2,21E-8	1,21E+11	0,21 (≠f(V)

The procedure of investigation of parameters Re/n-GaAs SBD by considering the R_s and N_{ss} effect begins by looking for V_0, E_F N_D, Φ_B values that can be extracted from dependence of capacitance on voltage [31-35]

$$\frac{d(1/C^2)}{dV} = \frac{2}{\varepsilon_s \varepsilon_0 q N_{Dapp} A^2} \quad (8)$$

where ε_s is the permittivity of the semiconductor (12,9 for GaAs), ε_0 *is* the permittivity of free space charge (ε_0= 8.85x10^{-14} F/cm). N_D is the concentration of doping (charge concentration) of the semiconductor (GaAs), A is the contact area of the diode.

With the using Eq.8 the experimental value of N_d has been calculated for low (10kHz) and high values (5MHz) of frequency (Fig.7)

$$N_d = \frac{2dV}{\varepsilon_s \varepsilon_0 q d(A^2/C^2)} \quad (9)$$

For Re/n-GaAs SBD by the using the intercept C^{-2}-V plot the value of potential barrier height (Φ_B) has been calculated at room temperature (500kHz, 50mV) [31-36]

$$\Phi_B = q(V_0 + E_F) \quad (10)$$

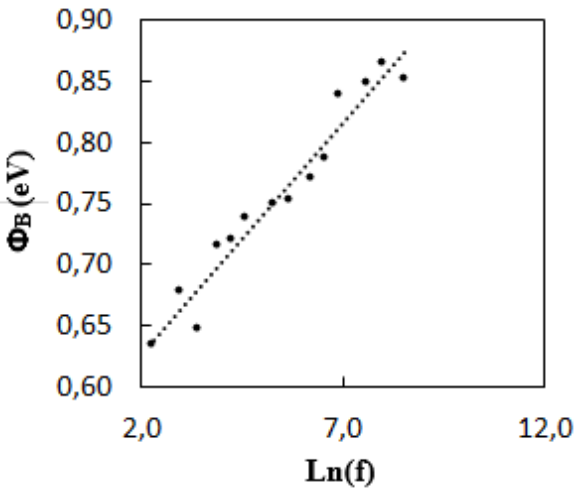

Fig.8. The dependence of potential barrier height (Φ_B) on frequency for Re/GaAs SBD.

Where V_0 is diffusion potential, the value of which from intersection of linear part of $(1/C)^2 - V$ characteristics was determined. Besides, the Fermi energy level (E_F) in the neutral region of n-GaAs was obtained as:

$$E_F = V_n = \frac{kT}{q} ln\left(\frac{N_c}{N_D}\right) \quad (11)$$

N_c is the effective density of states in non-degenerated conductance band of GaAs,

$$N_c = 2{,}5\mathrm{E} + 19 * (T/300)^{3/2} \left(\frac{m_e^*}{m_0}\right)^{3/2} \quad (12)$$

where m_e^* =0,068m_0 is the effective mass of the electron in GaAs [2,3] and m_0 (9.1×10^{-31} kg) is the rest mass of the electron.

The values of the barrier height obtained from the dependence C^{-2}-V differ from the values obtained from the $I - V$ characteristic. This discrepancy can be explained by the existence of an interfacial layer or surface states.

As is shown from Fig.8 the value of the potential barrier height dependent on frequency of test signal. Apparently, this dependence is due to the influence of the recharging of surface states [36].

CONCLUSION

The main parameters of the diode were studied based on the I-V, C-V and G/w-V characteristics measured at room temperature. The dependence I-V was measured in the voltage range $\pm$ 5V, the dependence of capacitance and conductance on voltage have been measured in the frequency range 10kHz-5MHz.The basic characteristics parameters such as Φ_B, n and R_s, R_i , R_{sh} have been calculated by using different methods (Cheung's, Norde's and Verner's methods) at room temperature and compared. The values of the parameters calculated by using different methods are slightly different, which indicates the difference between the selected and ideal model. Obtained result was attributed to the influence of lattice mismatch between the Re and GaAs on the formation of the barrier and surface states. On the basis of the $C - V$ and $G/\omega - V$ characteristics measured in a bias voltage 2V÷+5V and wide frequency range of test signal from 10kHz to 5000 kHz (50 mV) has been determined E_F, N_D , Φ_B, R_s N_{ss} and dependence on frequencies. It was revealed the contribution of surface states at low frequencies.

[1] *E.H. Rhoderick, R.H. Williams.* Metal–Semiconductor Contacts, Clarendon Press, Oxford, 1988.

[2] *V.I. Strikha.* Theoretical Bases of Metal-Semiconductor Contact Work, Naukova Dumka, Kiev, (1974) (in Russian).

[3] *S.M. Sze.* Physics of Semiconductor Devices, John Wiley & sons, New York, 1981.

[4] *I.M. Afandiyeva, Ş. Altındal, L.K. Abdullayeva, A.İ. Bayramova*. Self-assembled patches in PtSi/n-Si (111) diodes, Journal of Semiconductors, 2018,v.39, n5, pp.054002-1-7.

[5] *F. Taghizadeh, van Rensburg, P.J. Janse, K. Ostvar, et al.* Electronic properties and transformation kinetics of two prominent metastable defects introduced in GaAs during sputter deposition of Au Schottky contacts/Materials science in semiconductor processing / 2019,v.99, pp.23-27.

[6] *B. Kirezli, M. Ahmetoglu (Afrailov), A. Kara.* Electrical and optical properties of photodiode structures formed by surface polymerization of [P (EGDMA-VPCA)-SWCNT] films on n-GaAs/Journal of molecular structure, 2019,vol.1192,pp. 258-263.

[7] *Vezzoli, Andrea; Brooke, Richard J. Ferri, Nicolo et al.* Charge transport at a molecular GaAs nanoscale junction/Faraday Dıscussıons, 2018, vol. 210, pp. 397-408.

[8] *Chatterjee, Abhishek; K. Khamari, Shailesh ; S. Porwal.* Effect of Co-60 gamma-irradiation on the nature of electronic transport in heavily doped n-type GaN based Schottky photodetector/, 2018, vol.123, is.16, 161585.

[9] *B.S. Danilin.* Vakuum evaporation of thin films,M.Energiya, 1967, 312p.

[10] *Contelot, Fanny, Thomas, J. Robert, Seaman, John C.* Using porous iron composite (PIC) material to immobilize rhenium as an analogue for technetium. Environment InternationaL, 2019, vol. 128, pp. 379-389.

[11] *Littleton, A.H. Joshua Secco, A. Richard, Yong, Wenjun* et.al. Electrical resistivity and thermal conductivity of W and Re up to 5 GPa and 2300 K/Journal of Applied Physics,2019, 125,is.13,135901.

[12] *Tian, Bian; Yu, Qiuyue; Zhang, Zhongkai* et.al. Effect of magnetron sputtering parameters on adhesion properties of tungsten-rhenium thin film thermocouples Ceramics International , 2018, vol.4 p15-18.

[13] *Hasanli, Nijat; Gauquelin, Nicolas; Verbeeck, Johan*. Small-moment paramagnetism and extensive twinning in the topochemically reduced phase $Sr_2ReLiO_{5.5}$ Dalton Transactions, 2018, vol.47, is.44,pp.15783-15790.

[14] *Chia-Chien Lin.* Electrical and structural properties of Re/GaAs Schottky diodes/Journal of Applied Physics 85, 3893, 1999.

[15] *Durmus, H Yildirim, M., Altindal, S* .On the possible conduction mechanisms in Rhenium/n-GaAs Schottky barrier diodes fabricated by pulsed laser deposition in temperature range of 60-400K/ journal of materıals scıence-materıals ın electronıcs/ 2019,vol. 30, is.9, pp. 9029-9037.

[16] *Ya.Ya. Kudryk, V.V. Shynkarenko, V.S. Slipokurov* et al. /Determination of the Schottky barrier height in diodes based on Au–TiB_2–n-SiC 6H from the current-voltage and capacitance-voltage characteristics/ Semiconductor Physics, Quantum Electronics & Optoelectronics, 2014. V. 17, N 4. P. 398-402.

[17] *S.O. Tan, H. Uslu, O.C. Tecimer.* Electrical characterizations of Au/ZnO/n-GaAs Schottky diodes under distinct illumination intensities/J Mater Sci: Mater Electron. 2016, DOI 10.1007/s10854-016-4843-4.

[18] *Abdulkerim Karabulut.* Barrier height modification in Au/Ti/n-GaAs devices with a HfO2 interfacial layer formed by atomic layer deposition/ *Bull. Mater. Sci.* (2019) 42:5.

[19] *K. Bouzidi, M. Chegaar, M. Aillerie.* Solar cells parameters evaluation from dark I-V Characteristics/ Energy Procedia 18 (2012) 1601 – 1610.

[20] *H. Norde.* A modified forward I-V plot for Schottky diodes with high series resistance, *J. Appl. Phys.*1979:50;5052-5053S.

[21] *S.K. Cheung, N.W. Cheung.* Extraction of Schottky diode parameters from forward current-voltage characteristics. Appl. Phys. Lett. 49(2), p. 85-87. (1986).

[22] *J.H Werner.* Schottky barrier and pn-junction I/V plots -Small signal evaluation, Appl Phys A, 1988, 47:291-300.

[23] *N. Şimşir, H. Şafak, ÖF Yüksel, M. Kuş.* Investigation of current–voltage and capacitance–voltage characteristics of Ag/perylene-monoimide/GaAs Schottky diode. Curr Appl Phys 2012; 12: 1510-1514.

[24] *I.M Afandiyeva, R.F Babayeva.* The potential barrier height and profile of surface states of Re/n-GaAs Schottky barrier diode, Proc. of the 7th Int. Conf. MTP-2021: Modern Trends in Physics, dec. 15-17, 2021, BSU, Baku, Azerbaijan, pp.97-103.

[25] *A. Kaya, E.Marıl, Ş. Altındal, İ. Uslu.* The comparative electrical characteristics of Au/n-Si (MS) diodes with and without a 2% graphene cobalt-doped $Ca_3Co_4Ga_{0.001}O_x$ interfacial layer at room temperature/Microelectronic Engineering 149 (2016) 166–171.

[26] *P.N. Krylov.* Physical models of thermo-processed contact metal–semiconductors. Journal of Udmurt University, 2006, 4: 125.

[27] *M P. Shaskolskaya.*Crystallography. Moscow, Visshaya shkola, 1984.

[28] *C. Calandra, Giorgio Santoro.* Surface states of the (110) surface of GaAs,Journal of Physics C Solid State Physics 8(6):L86. 2001.

[29] *Erman Erdoğan[a], MutluKundakçı[b]* Room temperature current-voltage (I-V) characteristics of Ag/InGaN/n-Si Schottky barrier diode/ Physica B: Condensed Matter,Volume 506, 1 February 2017, Pages 105-108.

[30] *Haziret Durmuş and Ülfet Atav.* Extraction of voltage-dependent series resistance from I-V characteristics of Schottky diodes/ Appl. Phys. Lett. 99, 093505 (2011).

[31] *O.A. Soltanovich, N.M. Shmidt, E.B. Yakimov.* Frequency and temperature dependences of capacitance–voltage characteristics of InGaN/ GaN light-emitting structures with multiple quantum wells. Semiconductors, 2011, 45(2): 221.

[32] *S.J. Moloi, M. McPherso.* Capacitance–voltage behaviour of Schottky diodes fabricated on p-type silicon for radiation-hard detectors. Radiation Physics and chemistry, 2013, 85:73.

[33] *I.S. Yahiya, H.Y. Zahran, F.H. Alamri, M. Aslam.* Microelectronic properties of the organic Schottky diode with pyronin-Y: Admittance spectroscopy, and negative capacitance. Physica B: Condensed Matter, 2018, 543: 46.

[34] *G. Ersöz, ˙I. Yücedağ, Y. Azizian-Kalandaragh, I. Orak, S. Altındal.* Investigation of Electrical Characteristics in Al/CdS-PVA/p-Si (MPS) Structures Using Impedance Spectroscopy Method/ IEEE transactıons on electron devıces, v. 63, no. 7, July 2016,p.2948-2955.

[35] *F. Parlakturk, S. Altındal, A. Tataroğlu, M. Parlak, A. Agasiev.* On the profile of frequency dependent series resistance and surface states in Au/$Bi_4Ti_3O_{12}$/SiO_2/n-Si(MFIS) structures,p.81-88.

[36] *E.H. Nicollian and J.R. Brews.* MOS (Metal Oxide Semiconductor) Physics and Technology. New York, USA: Wiley, 1982, pp. 117–129.

Received: 01.10.2024

ISSN 1028-8546

2024, Vol. XXX, №3
Section: E

CONTENTS

1. Exact wave functions and dynamical symmetry group for the modified nonrelativistic ring-shaped Kratzer potential
Shakir M. Nagiyev, Könül Sh. Jafarova, Shovqiyya A. Amirova, Vefa A. Tarverdiyeva 3

2. Optical properties of semiconductor superlattices (Review)
S.A. Zalova 9

3. Thermophysical, dielectric and conductivity properties of plasma-modified composites based on PVDF dispersed with $BaTiO_3$ particles
I.S. Ramazanova, G.Kh. Guseynova, U.V. Yusifova, T.D. Ibragimov, A.F. Nuraliyev, F.F.Yahyayev 20

4. Investigation of the effect of sulphur on the properties of carbon nanotubes
Hasanov Rovshan Farhad 29

5. The connection between the energy and structural complexity of the matter, structural complexity origin of the electroweak boson masses as well as metabolism in living organisms
Fizuli Mamedov 33

6. The investigation of the voltage and frequency dependent electrical characteristics of Re/n-GaAs Schottky barrier diode using I–V, C–V and G/ω–V measurements
I.M. Afandiyeva, S.A. Yerishkin, E.A. Rasulov, S.I. Amirova 37

www.physics.gov.az